Master's thesis

2022

Børge Johannes Fagermyr

NTNU
Norwegian University of
Science and Technology
Faculty of Information Technology and Electrical
Engineering
Department of Electric Power Engineering

Børge Johannes Fagermyr

End-region losses in large hydropower generators

June 2022

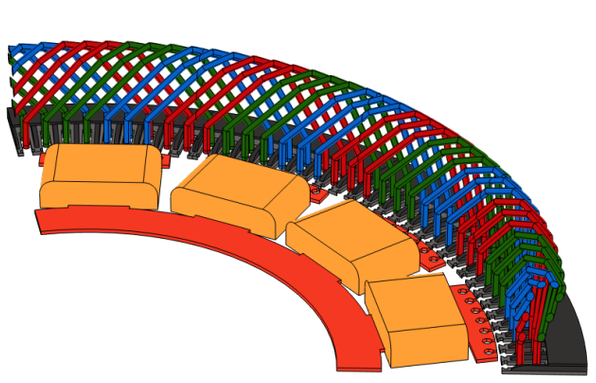

NTNU
Norwegian University of
Science and Technology

NTNU
Norwegian University of
Science and Technology

NTNU
Norwegian University of
Science and Technology

End-region losses in large hydropower generators

Børge Johannes Fagermyr

Energy and Environmental Engineering
Submission date: June 2022
Supervisor: Arne Nysveen
Co-supervisor: Zhaoqiang Zhang

Norwegian University of Science and Technology
Department of Electric Power Engineering

Abstract

Large generators have reportedly experienced partial overheating in the generator end region under certain operating conditions. Leakage flux in the generator end region can contain a significant axial component that penetrates the end part of the stator, thus creating high eddy current losses. Under loaded operation, the armature flux varies for different generator operation points, and the total flux is consequently dependent on the generator loading. Calculating the combined end region flux is a complex three-dimensional problem that can be solved using finite element method (FEM) modeling. This thesis aims to obtain the end region magnetic flux distribution and the end region power loss at selected operating points corresponding to leading, unity, and lagging power factor. For this purpose, a 3D FEM model is created based on a 100kVA synchronous generator.

The proposed 3D FEM model is a virtual generator model with an increased number of slots, thus reducing the complexity of the overall modeling process. More importantly, the proposed model drastically reduces the required computational power for obtaining results within a reasonable time frame. Anisotropic permeability is included in the 3D model of the lamination stack. Additionally, an improved B-H curve is used in modeling the stator iron. Simulation results show that the eddy current losses in the end region pressing structure are up to three times higher when the generator is under-excited than when the generator is loaded at unity power factor or at over-excitation operation. Similar conclusions are drawn for losses in the stator iron end region. Simulation results show that the axial component of the magnetic flux density in the end region is considerably higher at leading power factor compared to unity and lagging power factor for the same output power.

A loss measurement apparatus is constructed for experimental investigation on the effect of end region leakage flux. An Epstein frame with excitation controlled by a power supply is initially magnetized. A C-shaped core is then magnetized separately. With the C-core placed normal to the main field in the Epstein frame core, an Artificial Leakage Flux test is conducted. Stainless steel plates of varying thickness are placed in the airgap, emulating the press fingers and clamping plate found in the end region of synchronous generators. Incremental losses are obtained at increasing phase shifts between the main flux and leakage flux. The results show that the incremental losses are sensitive to variations in the angle between leakage flux and main flux.

Sammendrag

Store generatorer kan oppleve delvis eller fullstendig oppheting i generatorens endeområde under visse forhold. Lekkfluks i generatorens endeområde kan inneha en betydelig aksiell komponent som trenger gjennom endedelen av statorblikkpakken, og kan dermed skape høye virvelstrømstap. Ved normal drift varierer fluksen fra statorens endeviklinger for ulike driftspunkter, og den totale fluksen er følgelig avhengig av generatorbelastningen. Å beregne den kombinerte enderegionfluksen er et komplekst tredimensjonalt problem som kan løses ved hjelp av finite element method (FEM) modellering. Denne oppgaven har som overordnet mål å regne ut den magnetiske flukstettheten i enderegionen til en utvalgt generator, og regne ut tapene i enderegionen ved utvalgte driftspunkter. Disse er henholdsvis undermagnetisert drift, resistiv last og overmagnetisert drift. Til dette formål lages en 3D FEM modell basert på en 100kVA synkrongenerator.

Den foreslåtte 3D FEM-modellen er en virtuell generatormodell med et økt antall spor. Denne forenklingen reduserer kompleksiteten til modelleringsprosessen. Enda viktigere er at den foreslåtte modellen drastisk reduserer den nødvendige beregningskraften som er nødvendig for å oppnå resultater innenfor en rimelig tidsramme. Anisotrop permeabilitet er inkludert i 3D-modellen av statorblikkpakken. I tillegg brukes en forbedret B-H-kurve ved modellering av statorblikket. Simuleringsresultater viser at virvelstrømtapene i generatorens pressfingre og pressplate er opptil tre ganger høyere når generatoren er i undermagnetisert drift enn når generatoren er i henholdsvis overmagnetisert drift og ved resistiv belastning. Lignende konklusjoner trekkes for undersøkelser av tap i enderegionen av statorblikkpakken. Simuleringsresultater viser at den aksielle komponenten av den magnetiske flukstettheten i endeområdet er betydelig høyere ved ledende effektfaktor sammenlignet med andre lastsituasjoner.

Et tapsmålingsapparat er konstruert for eksperimentelle undersøkelser av effekten av lekkfluks i endeområdet. En Epstein-ramme magnetiseres først ut fra egen strømforsyning. Deretter magnetiseres en C-formet kjerne separat slik at denne kan etterlikne lekkfluks i enderegionen. Med C-kjernen plassert normalt på rammen, utføres en kunstig lekkflukstest. Rustfrie stålplater av varierende tykkelse plasseres i luftgapet for å etterligne pressfingrene og pressplaten i endeområdet til synkrongeneratoren. Inkrementelle tap måles ved økende faseforskyvning mellom hovedfluksen i rammen og lekkfluksen fra C-kjernen. Resultatene viser at de inkrementelle tapene er sensitive for variasjoner i vinkel mellom lekkfluks og hovedfluks.

Preface

This master thesis is written at the Department of Electric Power Engineering NTNU during the spring semester of 2022. The thesis is connected to HydroCen's ongoing research on hydro-generators.

First of all, I want to thank postdoc. Zhaoqiang Zhang for all the valuable support this semester, as well as in the work preceding this thesis. I want to thank professor Arne Nysveen for his valuable guidance and help in overcoming the many challenges faced in this project. Finally, I want to thank the service people at NTNU for all the help this semester as well as in the previous semester.

Kristiansand, 22-06-2022

Børge Johannes Fagermyr

NORGES TEKNISK-NATURVITENSKAPELIGE UNIVERSITET

NTNU

M A S T E R O P P G A V E

Kandidatens navn : Børge Johannes Fagermyr

Fag : **ELKRAFTTEKNIKK**

Oppgavens tittel (norsk) : Tap i enden av statoren til store vannkraftgeneratorer

Oppgavens tittel (engelsk) : End-region losses in large hydropower generators

Oppgavens tekst:
Large generators can experience critical overheating in the end-region of the stator. The laminated stator is mechanically supported by a frame. To hold the laminations together, there are press-rings at both ends of the stator stack. In this region, there are magnetic stray-fields causing excess losses and, in some cases, leading to overheating and damage of the stator. This project is part of a research project connected to HydroCen on loss modelling of large machines.

Create FEM model of a selected generator and investigate the magnetic field and induced losses in the end-region of the generator. Loss modeling based on experimentally obtained loss measurement data from the ring core specimen used in the specialization project. Further research using an experimental approach for characterizing the magnetic properties of laminated steel in an Epstein frame. Introduce a magnetic field normal to the main flux by including a C-core clamp-on to imitate the field in the end region of generators.

Further details to be clarified with the supervisors.

Oppgaven gitt	: 15. januar 2022
Oppgaven revidert:	: 18. juni 2022
Besvarelsen leveres innen	: 27. juni 2022
Besvarelsen levert	:
Utført ved (institusjon, bedrift)	: Inst. for elkraftteknikk/NTNU
Kandidatens veileder	: Postdoc Zhaoqiang Zhang
Faglærer	: Professor Arne Nysveen

Trondheim, 18. juni 2022

Arne Nysveen
faglærer

Contents

List of Tables

List of Figures

Chapter 1

Introduction

Research on end region losses in electrical machines is motivated by the severe potential consequences of generator failure related to core faults. It is well known that turbo generators' end region leakage flux will give rise to significant eddy currents in the generator end region [1]. Indeed, measures are taken specifically to screen the end region lamination sheets and pressing structures by the implementation of eddy current shields [2]. In salient pole synchronous generators, there are no eddy current screening shields. The impact of leakage flux related overheating in hydro generators is not well described in the literature.

Potential overheating in large generator end region due to the influence of leakage flux is a well-known phenomenon first recorded by the end of the 19th century following the rapid development of large rotating electrical machines with laminated cores [1]. In addition to electrical fault driving mechanisms, the influence of thermal and material factors are described in [1] emphasizing the complexity of fault initiation and growth. The finite element method is used in [3] for determining flux distribution and associated end region losses in large turbo generators. The complex nature of core fault development in turbo generators is described in [1].

Pressing structures such as pressing fingers and pressing plates are used to maintain sufficient continuous pressure on the stator lamination stack, thus ensuring a rigid construction capable of withstanding all mechanical forces in generator operation. The press plate also serves a valuable function of shielding the stator core back iron from the end region leakage flux[4]. The pressing structure in the generator end region will be subjected to leakage flux with a significant axial component. Consequently, eddy current power losses in the support structure can be significant under certain operating conditions, as emphasized in [5][3]. End region loss distribution analysis in [3] shows that the magnetic flux does not penetrate the press plate by much due to the skin effect. It is found that the impact of armature mmf is more influential on the loss density in the pressing plate than the field mmf.

As the influence of end region leakage flux in salient pole synchronous generators is not well described in the literature, two approaches are proposed in this thesis. First, a 3D FEM model is created with the aim of calculating the end region losses by simulating different operation points. Secondly, further research on end region leakage flux is conducted using an experimental approach to support the simulation results. Conditions emulating end region leakage flux created in an Artificial Leakage Flux test.

Chapter 2

Theory

In this section fundamental concepts related to synchronous machines is presented in addition to an introduction to relevant core loss prediction methods. Relevant concepts related to synchronous generators is presented in section 2.1. FEM modeling principles are presented in section 2.2, and end region losses in synchronous machines is presented in section 2.3. Finally, core loss estimation methods originally written for the specialization project preceding this thesis Fagermyr [6] are presented in section 2.4.

2.1 Synchronous generators

A synchronous generator consists of a rotation part called the rotor, and a stationary part called the stator. The two most common synchronous machines are the round rotor and salient pole synchronous machines. Round rotor machines are typically used in turbo generators. The round rotor synchronous machines operate at high rotational speed with a low number of poles. Salient pole synchronous machines have many poles, and lower angular velocity to match the system frequency [7]. Salient pole synchronous machines are commonly used in large hydropower plants. Figure 2.1(a) and Figure 2.1(b) are 2D illustrations of an example salient pole synchronous machine.

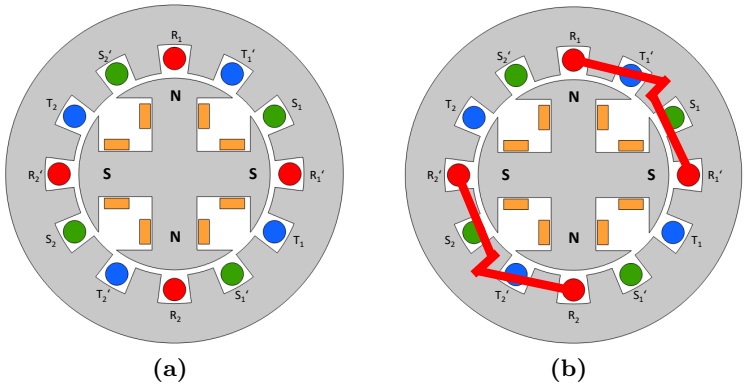

Figure 2.1. Example of a 4 pole 12 slot salient pole synchronous generator. Illustration of: (a) an arbitrary cross section; (b) with end winding for phase R included.

Magnetic rotor poles are created using dc excitation current, as illustrated in the 4-pole machine in Figure 2.1(a,b). In the stator, voltage is induced in the stator windings by the rotor magneto-motive force (mmf). The three phases R, S, and T in Figure 2.1 are color-coded red, green and blue, respectively. Each phase consists of two separate windings. For phase R, R_1 refers to the first winding in phase R, with the current direction in the $\hat{z}$-direction. The reverse current for the first R-phase winding is denoted R_1' with the current direction in the negative $\hat{z}$-direction.

Neglecting cooling channels, the 2D representation in Figure 2.1(a) represents all cross-sections in the machine stacking length, except the generator end region. The winding connections are made in the generator end region, exemplified for phase R in Figure 2.1(b). Similar connections are made for all windings in the end region.

In contrast to round rotor machines where the radial airgap length is uniform along the rotor outer circumference, salient pole synchronous machines have a non-uniform air gap length. In Figure 2.1(a,b), the airgap length can be observed to be minimal along the rotor poles and maximum in between rotor poles. The non-uniform airgap poses several modeling challenges that are not present in round rotor machines. The two-reaction theory provides a valuable simplification to the modeling challenges by introducing the dq-frame. The d-axis is placed along the rotor mmf, which is directed along a rotor north pole. The q-axis is lagging the d-axis with 90° electrical, corresponding to 45° mechanical in the case of a 4-pole machine. The induced no-load voltage is thus directed along the q-axis in the per phase phasor diagram representation of a synchronous generator.

Two constant reactances X_d and X_q can be defined since the airgap reluctance is constant along the d-axis and q-axis. The reluctance in the d-axis is drastically lower than in the q-axis because of minimal airgap length. Reactance is inversely proportional to

the associated reluctance, and so it follows that $X_d > X_q$ [7]. Similarly, the armature current is resolved into one component $\bar{I}_q$ in phase with the q-axis and another component $\bar{I}_d$ in counter phase with the d-axis. The per-phase phasor diagram for a salient pole synchronous generator can be drawn as illustrated in Figure 2.2 at lagging power factor.

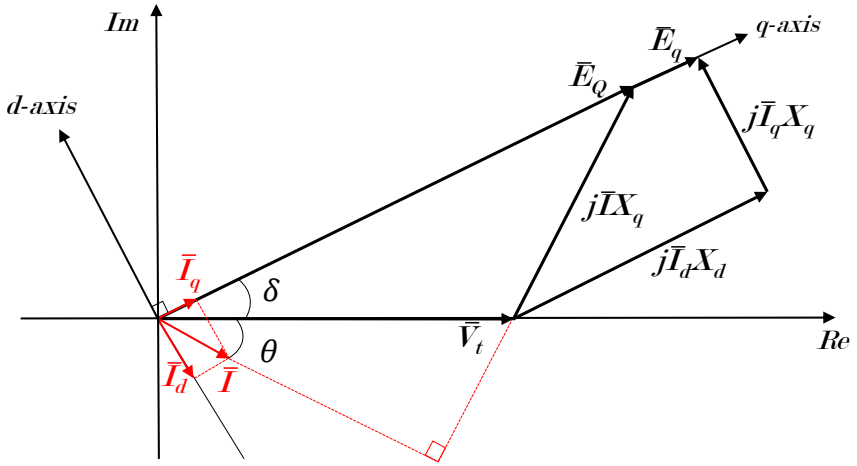

Figure 2.2. Phasor diagram of a salient pole synchronous generator operating at lagging power factor. Inspired by [7].

In Figure 2.2, the terminal voltage $\bar{V}_t$ is chosen as reference. Armature current $\bar{I}$ is lagging the terminal at an angle θ referred to as the load angle. The internal voltage $\bar{E}_q$ is at an angle δ referred to as the power angle. The power angle must be determined to calculate the internal voltage and the decomposed currents $\bar{I}_q$ and $\bar{I}_d$. To accomplish this, $\bar{E}_Q$, which is directed along the q-axis at an angle δ, is calculated.

$$\bar{E}_Q = \bar{V}_t + jX_q\bar{I} \tag{2.1.1}$$

Once the power angle is obtained, the direct and quadrature current is found using the relationship in equation 2.1.2, which is derived from the phasor diagram in Figure 2.2.

$$\begin{aligned} \bar{I}_d &= |\bar{I}|sin(\delta+\theta)\angle(\delta-90°) \\ \bar{I}_q &= |\bar{I}|cos(\delta+\theta))\angle\delta \end{aligned} \tag{2.1.2}$$

From the phasor diagram in Figure 2.2 it is clear that the internal voltage $\bar{E}_q$ is obtained using the relationship defined in Equation 2.1.3.

$$\bar{E}_q = \bar{V}_t + jX_d\bar{I}_d + jX_q\bar{I}_q \tag{2.1.3}$$

2.2 Principles of FEM-modelling

An important aspect to consider in generator design is the relationship between the number of poles and the number of slots in the stator. FEM modeling of a synchronous generator is thus initiated by examination of the machine number of slots per pole and phase q given in Equation 2.2.1.

$$q = \frac{N_s}{3N_p} \tag{2.2.1}$$

In Equation 2.2.1 N_s is the number of stator slots, N_p is the number of poles. An integral slot machine is a configuration where q is an integer. A fractional slot machine refers to machines where the number of slots per pole and phase is not divisible by any real number.

Rotating electrical machines can be modeled using the finite element method (FEM). The principles presented in this section are based on modeling a 2D representation of a salient pole synchronous machine, as the principles are also valid in 3D modeling.

Typically, a two-dimensional model of an arbitrary cross-section of the machine is used for FEM modeling of synchronous machines. This approach can be beneficial as a machine cross-section represents the total machine stacking length. Accurate results can be obtained for machine performance using the net machine length in a post-processing process.

The model size can be significantly reduced by utilizing exciting symmetry lines. For modeling an integral slot machine, the model can be reduced to one pole pair since there is a periodicity among adjacent pole pairs [8]. Thus, the 12-slot four-pole model in Figure 2.1 can be divided into two identical sectors, corresponding to half of the total machine and two poles, illustrated in Figure 2.3(a). Further model size reduction is possible if similar symmetry lines are present in the stator winding arrangement. In the case of the example integral slot, the model can be reduced to a single pole since the number of stator slots is divisible by the number of poles [8]. Model reduction to one pole is shown in Figure 2.3(b).

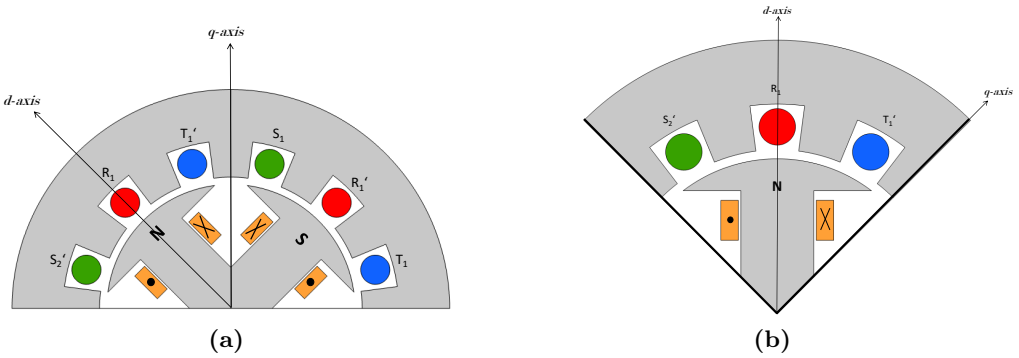

Figure 2.3. Illustration of the model size reduction concept using a 4 pole 12 slot machine. Figure illustrating the model reduced to: (a) one pole pair; (b) one pole.

Boundary conditions are applied to the sector model utilizing model symmetry. Anti-periodic boundary conditions are assigned to the boundary along the q-axis as all flux lines exciting this boundary are assumed to be entering the boundary located one complete sector angle in the clockwise direction from the q-axis.

2.3 Laminated iron core and end region losses

The stator core consists of electrical steel sheets assembled in stacks, with insulation between separate sheets. An illustration of an assembly of electrical sheets is presented in Figure 2.4.

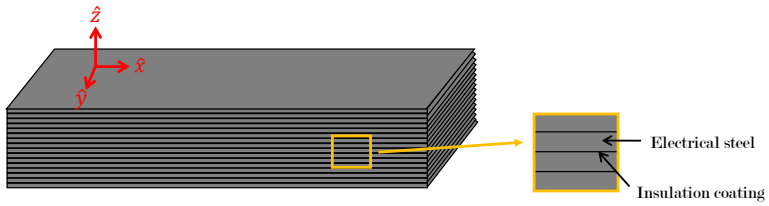

Figure 2.4. Illustration of an arbitrary iron core.

In Figure 2.4, the lamination plane is indicated by reference vectors $\hat{x}$ and $\hat{y}$. In this example figure, $\hat{x}$ is directed in the rolling direction. Normal to the xy-plane is the reference vector $\hat{z}$. In Figure 2.4, the magnetic permeability is high in the rolling direction. The magnetic permeability is, however, low in the normal direction because of the insulation coating separating sheets. Similarly, the electrical conductivity of electrical steel is high in the rolling direction and low in the normal direction. In an electrical machine, the magnetic flux density is normally in the $\hat{x}\hat{y}$-plane for the total machine stacking length, except in the end region. This illustrated in Figure 2.5.

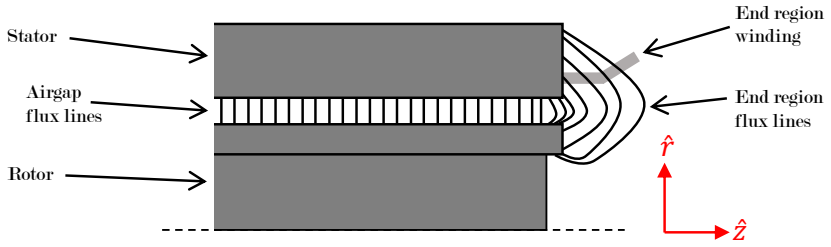

Figure 2.5. Schematic drawing of a 2D representation of an arbitrary generator end region under no load operation.

Figure 2.5 illustrates how the airgap flux is directed in the radial direction for the active generator length. In reality, the airgap flux also consists of a ϕ-component. Consequently, the magnetic flux density is in the lamination plane, and the available eddy currents paths are minimal. However, this is not the case in the generator end region. From Figure 2.5, it can be observed that leakage flux from the rotor enters the stator end core with a considerable axial component in the $\hat{z}$ direction. As eddy currents form to oppose the magnetic field from which they originate, an axial flux density in Figure 2.5 corresponds to magnetic flux in the $\hat{z}$-direction in Figure 2.4. The outer sheets are thus subjected to large circulating currents in the plane of laminations. Consequently, eddy current losses can be significant in the end region stator core. Section 2.4 and section 2.4.2 are from Fagermyr [6].

Under loaded operation, the end region flux is influenced by leakage flux from the stator end winding. The leakage flux in the armature windings originates from the load current,

which depends on the generator operation point. Interaction between the rotor flux and the stator flux is not included in Figure 2.5.

2.4 Core losses

Non-oriented electrical steel is used in high-performance electrical machines because its beneficial magnetic properties provide high permeability and low power loss. Accurate prediction of core losses is essential in machine design and should apply in different loading situations. Excising loss models are, however, developed for a wide range of different purposes and constraints.

2.4.1 Loss estimation methods

The most commonly used approaches for core loss predictions in electrical machines are models based on the Steinmetz equation, separation of total losses into hysteresis and eddy current losses, loss separation by magnetizing process, or mathematical hysteresis models [9]. Core loss models based on the Steinmetz equation are used in fast core loss prediction under the assumption of sinusoidal flux density in the core. The Steinmetz equation is given in Equation 2.4.1 [10].

$$P_{tot} = k f^{\alpha} B_m^{\beta} \tag{2.4.1}$$

In Equation 2.4.1 the coefficients k, α and β are material constants derived from experimental data, B_m is the maximum magnetic flux density and P_{tot} is the total core loss density. Many core loss models are based on Equation 2.4.1 and the principle of loss separation into eddy current and hysteresis losses. The two-term model is widely acknowledged for providing fast core loss prediction. There are, however, reportedly significant discrepancies between the two-term loss model and measured core losses. A three-term model containing an additional term for excess losses is often used to account for this difference. The three-term model in Equation 2.4.2 separates the total losses into hysteresis losses P_h, eddy current losses P_e and excess losses P_{exc} [11].

$$\begin{aligned} P_{tot} &= P_h + P_e + P_{exc} \\ &= K_h f B_m^2 + K_e f^2 B_m^2 + K_{exc} f^{1.5} B_m^{1.5} \end{aligned} \tag{2.4.2}$$

In Equation 2.4.2 K_e is the eddy current loss coefficient, K_h is the hysteresis loss coefficient and K_{exc} is the excess loss coefficient. B_m is the maximum magnetic flux density for a given field strength, and f the frequency.

2.4.2 Calculations for investigation of material properties

For a closed magnetic circuit, the magnetic field strength $H(t)$ is proportional to the current in the excitation coil and the number of turns N, following the relationship in Equation 2.4.3.

$$H(t) = \frac{N}{l_{eff}} i(t) \tag{2.4.3}$$

In Equation 2.4.3, l_{eff} is the effective length of the magnetic circuit. The current $i(t)$ is the current in the excitation coil. The voltage induced in the measuring coil $u(t)$ is caused by the time rate of change in iron core flux ϕ, described in Equation 2.4.4.

$$u(t) = N\frac{d\phi(t)}{dt} \tag{2.4.4}$$

Assuming homogeneous flux density distribution in the iron core, the flux density at a given time instant is equal to the product of magnetic flux ϕ through the cross-sectional area and the core cross-sectional area A_c. Thus, the induced voltage can be described as in Equation 2.4.5.

$$u(t) = NA_c\frac{dB(t)}{dt} \tag{2.4.5}$$

From Equation 2.4.5 it can be observed that the assumption of sinusoidal flux density can easily be verified by visual inspection of the induced voltage waveform. Rearranging Equation 2.4.5, the magnetic flux density $B(t)$ can be obtained as described in Equation 2.4.6.

$$B(t) = \frac{1}{NA_c}\int u(t)dt \tag{2.4.6}$$

Numeric data is obtained in a voltage and current measurement. From the measured current and voltage for a given time interval, dt is the total measuring time relative to the sample length of numeric data points. The magnetic field strength is found from the measured data described in Equation 2.4.3. The magnetic field strength and flux density are then plotted to obtain the BH-loop. Combining the tipping point of several hysteresis loops, i.e. points of $B_{max}(H_{max})$, yields the final BH-curve for a specific frequency.

Chapter 3

Methodology

The methodology in this thesis is sectioned into two main parts related to the 3D modeling of the synchronous generator and a laboratory test of artificial leakage flux. First, the 3D synchronous generator model construction is described in section 3.1. Secondly, a description of the test setup for investigating artificial leakage flux is given in section 3.2.

3.1 FEM modelling of the synchronous generator

This section explains the steps taken to construct the final 3D sector model of the synchronous generator. A brief description of the real generator and justifications for geometrical changes to the design is given in section 3.1.1, in addition to a detailed description of model construction. The complete 3D model is presented in section 3.1.2. The mesh is described in section 3.1.3. Implementation of operating points to evaluate end region losses in the 3D model is described in section 3.1.4. Experimental investigation of the magnetic properties is presented in section 3.1.5, based on results from the work preceding this thesis Fagermyr [6].

3.1.1 Virtual Synchronous Machine Model

The generator sector model is based on data sheet information of an existing synchronous generator hereafter referred to as RSM (*Real Synchronous Machine*). Figure 3.1(a) shows the RSM stator with the rotor removed. Figure 3.1(b) shows the RSM rotor.

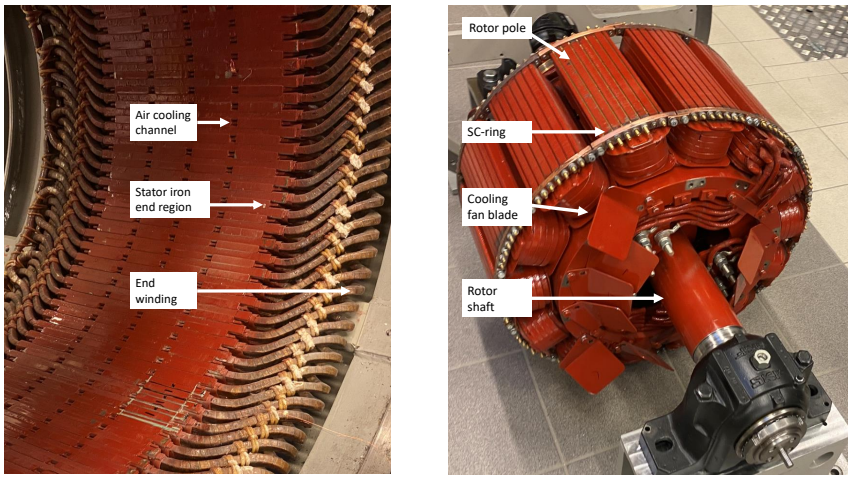

(a) **(b)**

Figure 3.1. RSM: (a) stator; (b) rotor.

In Figure 3.1(a) the stator end windings and stator lamination stack end region is clearly visible. The fan blades in Figure 3.1(b) are tilted out of the original position. A summary of data sheet information on the RSM is included in Table I.

TABLE I. RSM data sheet values

Dimension	Value	Unit
Nominal power	90	kW
Rated kVA	100	kVA
Rated voltage	400	V
Rated speed	428	rpm

A virtual FEM model of the real synchronous machine is created using software from COMSOL Multiphysics. The FEM model is referred to as VSM *(Virtual Synchronous Machine)*. The FEM model is not an exact virtual representation of the real generator as some geometrical adjustments are made to the original design. The most predominant difference between the RSM and the VSM is the number of stator slots. In VSM, the

number of slots is increased from 114 in the RSM to 126 in VSM. All geometrical differences are directly related to this adjustment.

The motivation for modifying the number of stator slots is based on the conclusions drawn in section 2.2, where the nature of integral slot windings is found to be highly beneficial for FEM modeling. Indeed, modification is required to achieve a model size reduction suitable for FEM simulations with reasonable computational power. A comparison of stator dimensions for the RSM and VSM is given in Table II.

TABLE II. Geometrical comparison of stator dimensions

Dimension	Parameter	RSM	VSM	Unit
Stator outer diameter	D_{so}	780.00	780.00	mm
Stator inner diameter	D_{si}	650.00	650.00	mm
Axial stacking length	L_m	217.5	217.5	mm
Stator tooth inner width	w_t	11.26	10.19	mm
Slot radial length	h_s	33.50	33.50	mm
Slot width	w_s	8.50	7.69	mm

In Table II, *inner* and *outer* referrers to *closer* and more *outlying* position in radial direction from center of rotation respectively. No changes are applied in the radial direction. The geometrical changes only affect the dimensions with a circumferential component. The circumferential components are reduced by a scaling factor equal to the relative change in the number of slots, corresponding to a change of 10.53%. For both models, the rotor dimensions are identical. Selected quantities are given in Table III.

TABLE III. Generator model comparison of derived values.

Dimension	RSM	VSM	Unit
Slots per pole and phase, q	2.71	3	-
Number of poles, N_p	14	14	-
Number of slots, N_s	114	126	-
Slots per pole	8.14	9	-
Pole pitch, τ_p	25.71	25.71	deg
Slot pitch, τ_s	$\frac{360}{114}$	$\frac{360}{126}$	deg

The RSM is a fractional slot machine with an average coil pitch of 7.13 slots. It follows from the adjustments in total slot number that the winding arrangement in the VSM will be slightly simplified. In a full-pitch winding, the coil pitch in number of slots would be 9, as stated in Table III. A single slot coil pitch reduction best resembles the original generator winding. The resulting winding pattern is illustrated in Table IV with numbers indicating each separate slot.

TABLE IV. Winding pattern for the VSM where τ_p is the pole pitch

	Slot number								
	1	**2**	**3**	**4**	**5**	**6**	**7**	**8**	**9**
Top layer	-R	-R	-R	S	S	S	-T	-T	-T
Bottom layer	-R	-R	S	S	S	-T	-T	-T	R
	$\leftarrow$				τ_p				$\rightarrow$

In Table IV a negative sign is indicating reversed current direction. The minimum 2D model of the RSM is presented in Figure 3.2(a) with fractional slot winding layout presented in tabular form in A.2. Figure 3.2(b) is the minimum size 2D model for the VSM with winding layout given in Table IV.

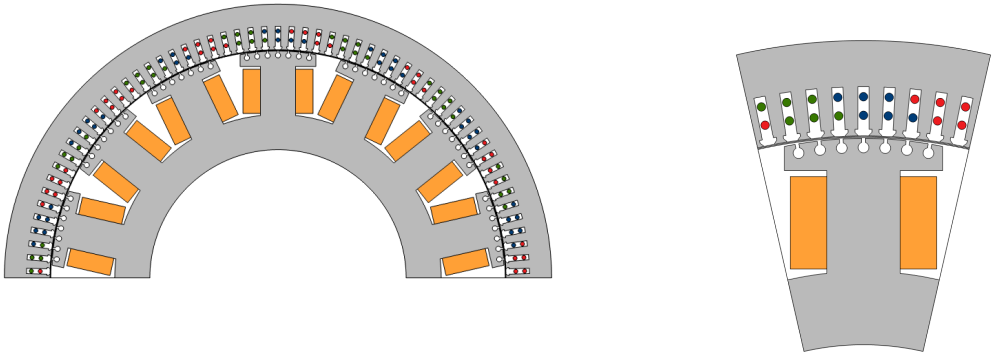

(a) **(b)**

Figure 3.2. Cross sectional representation of the minimum model size of reduced models for: (a) 114 slot 2D RSM model; (b) 126 slot 2D VSM model.

As illustrated in Figure 3.2(a) and Figure 3.2(b), the minimum possible model reduction is corresponding to only one pole pitch for the suggested VSM. If instead the RSM had been modeled, the minimum possible reduction based on available symmetry lines would be seven poles corresponding to half of the machine.

The VSM model is based on the parameters in Table II. The model is created using inbuilt operations available in the COMSOL Multiphysics model builder. Initially, only a cross-sectional 2D representation of the VSM is created for the stator lamination stack, rotor iron, field winding and stator windings. The 2D VSM model is used to validate the selected operation points.

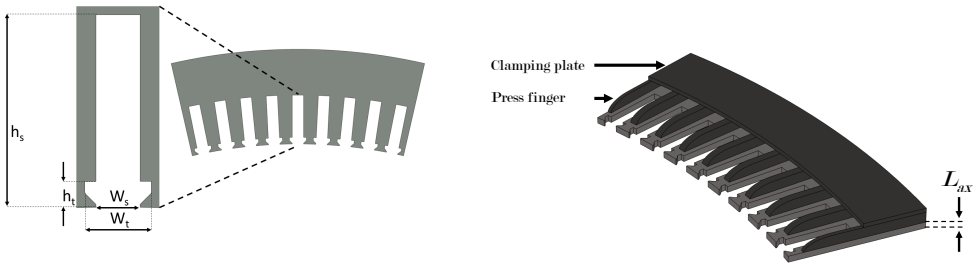

(a) **(b)**

Figure 3.3. Stator iron geometry for the COMSOL model in: (a) 2D VSM model; (b) 3D VSM model.

Figure 3.3(a) shows how a 2D single sheet is created using only the stator tooth dimensions in addition to the inner and outer diameter. The stator tooth dimensions are included in Table II. The stator slots are distributed across the stator iron inner circumference with equal spacing between adjacent slots. The angle of displacement is determined by the slot pitch τ_s in Table III. The 3D model of the stator iron in Figure 3.3(b) is simply the 2D model in Figure 3.3(a) extruded L_{ax}[mm] in the generator axial direction. For

the 3D model L_{ax} is chosen to be 3 mm, corresponding to 6 sheets with a thickness of 0.5mm. Press fingers and clamping plate is included in the 3D VSM, as shown in Figure 3.3. Losses will be evaluated in the pressing structure. The rotor is modeled using the real rotor using known dimensions from the manufacture datasheet. Figure 3.4 shows the complete sector model rotor with field winding.

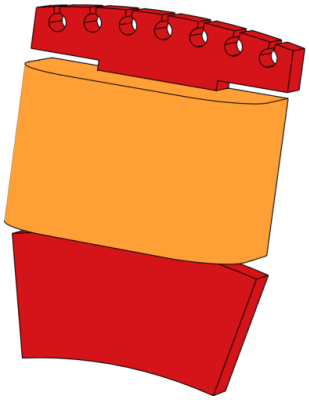

Figure 3.4. The VSM rotor model with rotor iron in red and field winding in orange color.

From Figure 3.4 it is clear that some simplifications have been made in constructing the 3D model. The damping bars and short-circuiting ring, visible in Figure 3.1(b), are excluded in the VSM. The effect is assumed negligible on the end region flux density as the generator model will operate at predefined steady-state operation points and not under fault situations. The field winding is formed as a single block multi-turn block with 35 turns, assuming even current density in the field winding block. This simplification does not capture the complexity of the RSM field winding in Figure 3.1(b). However, it is concluded that simplifications regarding the field winding are preferable as the computational strain is drastically increased if each field winding coil is modeled.

The stator windings are made using the winding layout in Table IV to form the distributed double layer winding with reduced coil pitch. The armature windings for the VSM are shown in Figure 3.5(a), and the total winding layout is illustrated in Figure 3.5(b).

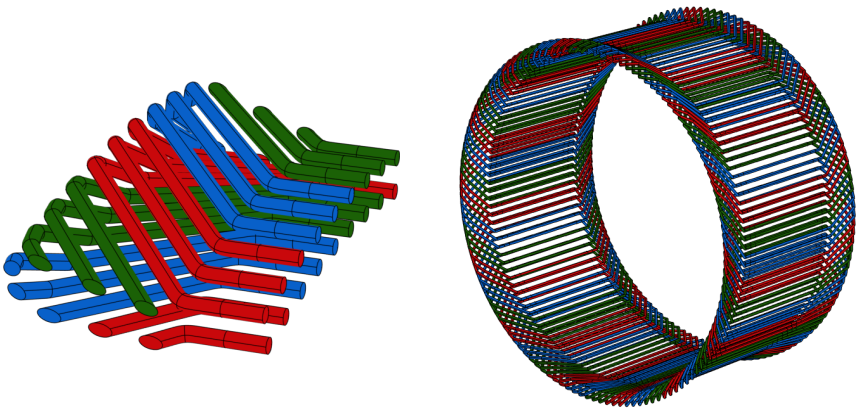

(a) **(b)**

Figure 3.5. Stator windings in the VSM for: (a) VSM sector model; (b) illustration of the total generator winding layout.

In Figure 3.5(a) and Figure 3.5(b) phase R, phase S and phase T is indicated with colors

red, blue and green respectively. The current direction is not visualized but is described for the VSM windings in Table IV.

The generator winding in Figure 3.5(b) is created by rotating the sector winding model in Figure 3.5(a) along the generator circumference. The mirror function in COMSOL is finally used to reflect the resulting winding to the other side, thus completing the total generator winding. It is worth noting that the geometry in Figure 3.5 is included only for illustrative purposes.

A circular cross-section is used to create the armature windings in the VSM. In COMSOL, this is achieved by sweeping a cross-sectional representation of the armature coil along a predefined polygon. This is a simplification as the windings in the RSM are rectangular. However, the approach is beneficial from a modeling perspective regarding model development and creating a mesh with satisfactory quality. The diameter of the armature windings is close to the width of the original rectangular coils.

3.1.2 The complete 3D VSM model

Available symmetry planes in VSM provides the opportunity to reduce the model size from 14 poles to a single-pole, in accordance with the theory presented in section 2.2. The complete 3D VSM model is presented in Figure 3.6(a). Figure 3.6(b) is an illustration of total machine geometry.

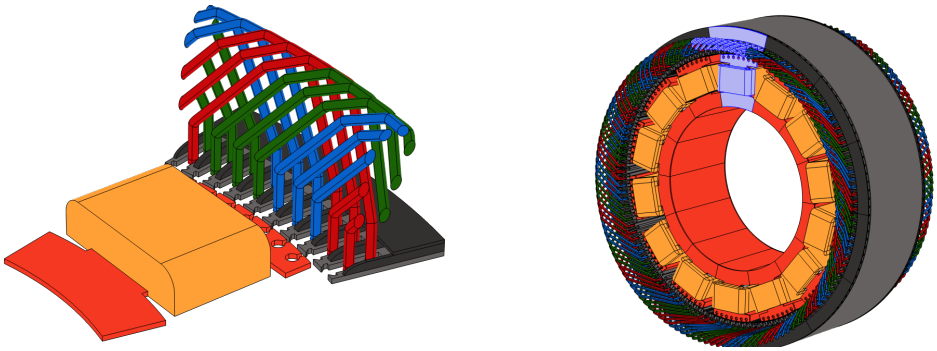

(a) **(b)**

Figure 3.6. The complete 3D VSM model: (a) single pole; (b) multiple poles from duplicating the single pole model.

Combining the stator iron, stator windings, and the rotor model completes the modeling of the 3D VSM model. The model is shown in Figure 3.6. For illustration, the 3D VSM model can be duplicated around the center of rotation to illustrate the benefit of modeling a single one-pole sector, as shown in Figure 3.6(b), where the 3D VSM model is highlighted.

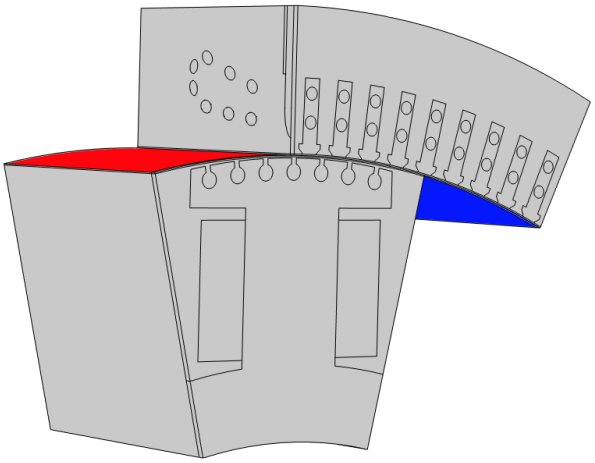

Figure 3.7. The 3D VSM model identity boundary pair.

Figure 3.7 illustrates the model separation into rotating and stationary domains. Naturally, stator domains are modeled to be stationary. Aniperiodic boundary conditions are applied in the boundary separating the stationary and rotating domains, illustrated in Figure 3.7 with the colors blue and red, respectively. Similarly, antiperiodic boundary conditions are applied to each side of the model Figure 3.7.

3.1.3 Meshing of the VSM

The 2D VSM model mesh consists of 30 000 elements with an average element quality of 84% considering the mesh element skewness, which indicates the symmetry level within each element. The mesh is presented in Figure 3.8 with the highlighted airgap and stator windings mesh.

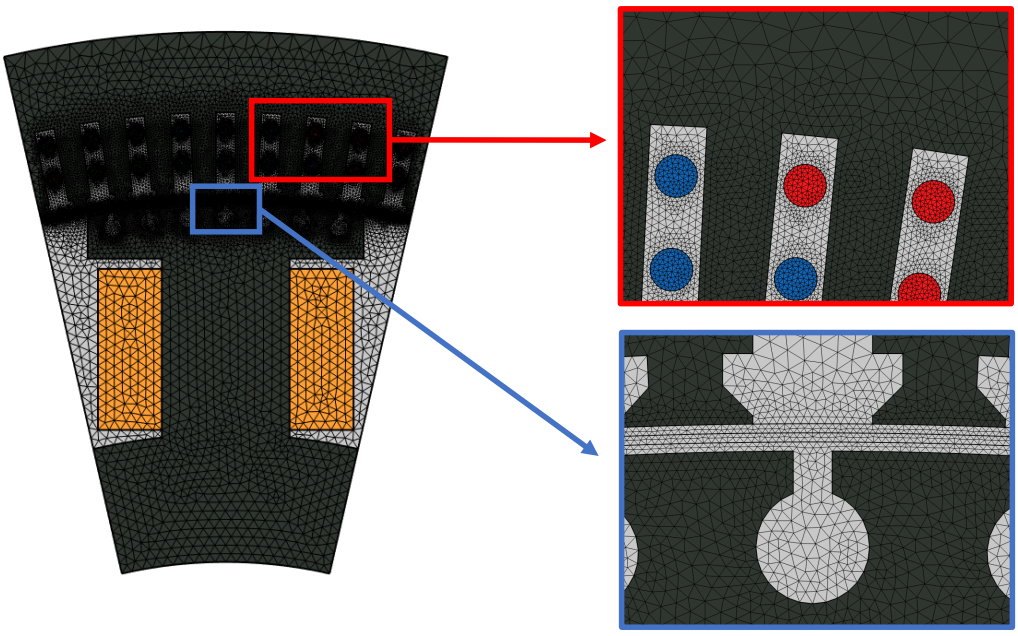

Figure 3.8. The 2D VSM model mesh with enlarged areas. Red box: Stator windings mesh; Blue box: Airgap mesh.

The 3D VSM model mesh is created with a total number of 606 000 elements, with an average quality of 63% based on the skewness measurement of the elements. Mesh elements are far from uniformly distributed in the 3D model compared to the 2D model mesh for the 2D VSM model. In the 3D model, a fine mesh is used only in the stator, rotor, and airgap domains. The mesh is presented in Figure 3.9, in which the airgap and pressing structure mesh are enlarged.

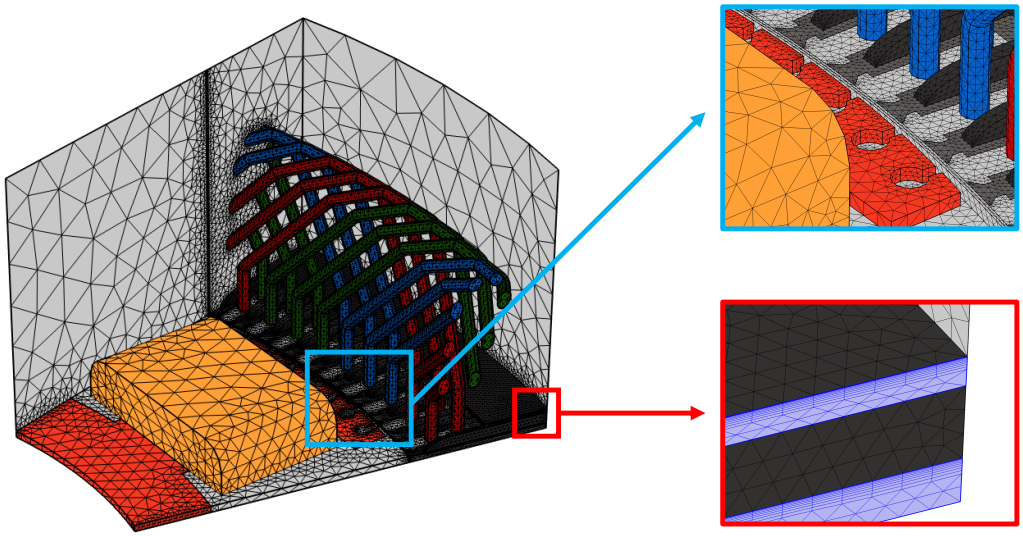

Figure 3.9. The 3D VSM model mesh with enlarged areas. Red box: Clamping plate and stator iron mesh highlighted; Blue box: Air gap domain mesh. Selected boundaries are partly removed for visualisation purposes.

Several aspects affect the decisions taken for creating the model mesh. A denser mesh is required to obtain accurate results in domains where end region losses are investigated. Thus, a fine mesh is created in the pressing structure and stator iron. Another essential aspect to consider is the computational strain and simulation time. For meshing of the model, a coarser mesh is applied to regions that are not considered important for evaluating end region losses. A fine mesh is used in the airgap domains and stator windings.

3.1.4 Implementation of Operating Points

In order to determine the end region losses under different loading situations, three different operation points are selected. The operation points are found from measured values in the generator data sheet for under-excitation, unity power factor, and over-excitation. The selected operation points are shown in Figure 3.10.

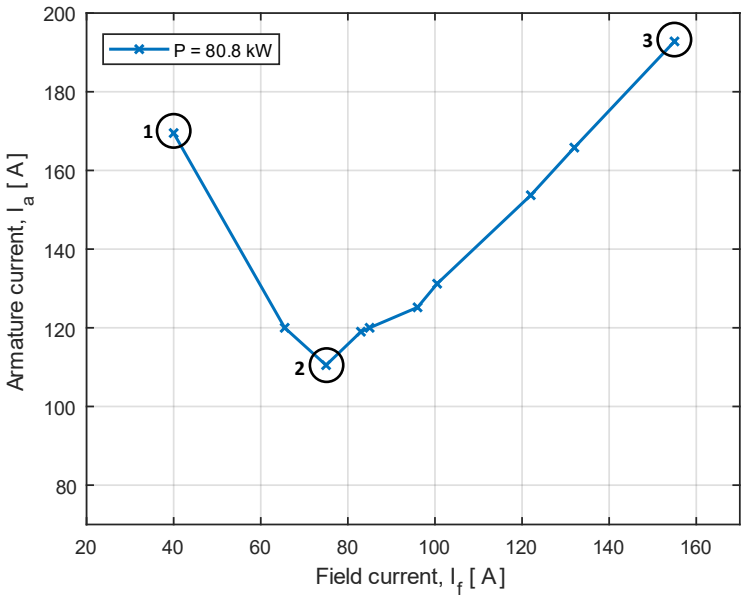

Figure 3.10. Characteristic full load V-curve for the RSM with selected operation points for the VSM. I_a is the per phase armature RMS current. 1: leading pf, 2: Unity pf, 3: lagging pf

In Figure 3.10 the operation points are illustrated with the associated V-curve for the generator operating at 80.8kW. More information on the selected operating points is provided in Table V including derived values of interest for the analysis.

TABLE V. Values of interest related to the operating points

Case	Operation	I_a [A]	I_f [A]	S [kVA]	pf [-]	θ [deg]
1	Leading	169.5	40	117	0.69	47
2	Unity	110.5	75	81	1.00	0
3	Lagging	192.8	155	134	0.60	-53

The phasor diagram of the operating point is given in Figure 3.11(a) for leading power factor, in Figure 3.11(b) for unity power factor and in Figure 3.11(c) for lagging power factor. The phasor diagrams quantities are calculated using the methods described in section 2.1 with available data sheets values for direct and quadrature synchronous reactance. Calculated phasor diagram values are included in A.4.

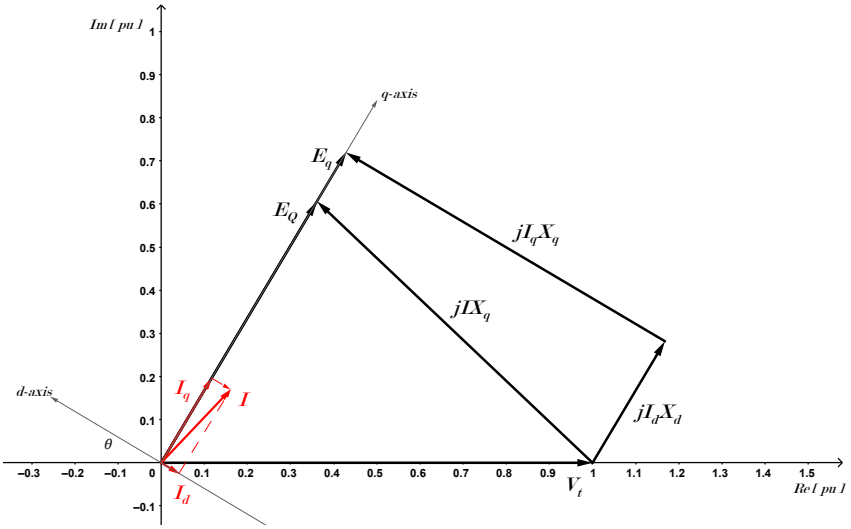

(a)

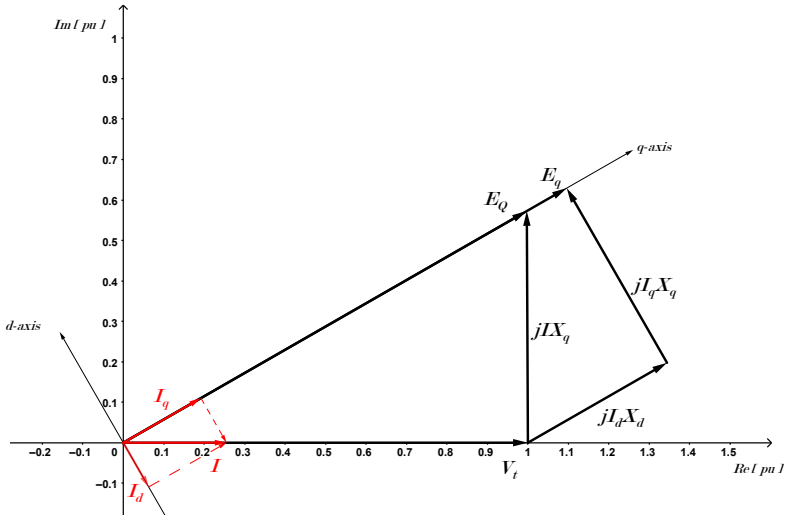

(b)

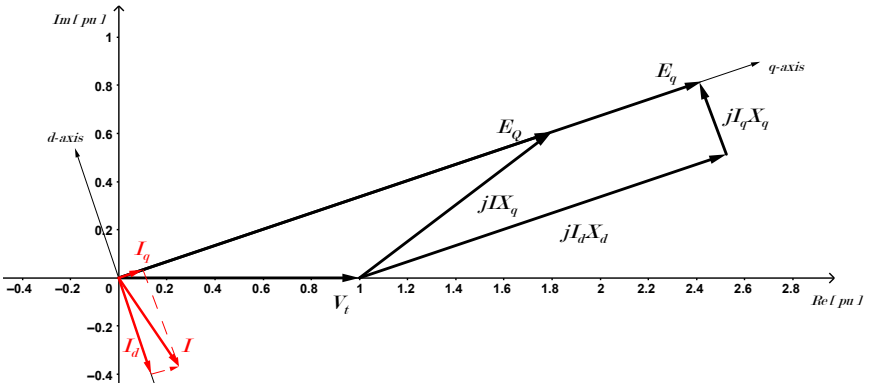

(c)

Figure 3.11. Phasor diagrams for the selected operating points corresponding to: (a) leading power factor; (b) unity power factor; (c) lagging power factor

It is important to note that the operation points from Table V, with associated phasor diagrams in Figure 3.11, illustrate the operation point of the RSM model. Because of the mentioned differences between the 114 slot RSM and the 126 slot VSM model, the operation points can not be directly implemented in the 3D VSM. Consequently, an alternative approach is used for implementing the operating points corresponding to Table 3.10. The method is initiated by defining stator currents in the 2D VSM model as shown in Equation 3.1.1.

$$\begin{aligned} i_A(t) &= \hat{I}_a cos(\omega t - \lambda), \\ i_B(t) &= \hat{I}_a cos(\omega t + 120^\circ - \lambda), \\ i_C(t) &= \hat{I}_a cos(\omega t - 120^\circ - \lambda). \end{aligned} \tag{3.1.1}$$

In Equation 3.1.1, $\hat{I}_a$ is the armature current peak derived from Table V. For obtaining valid operation points for the VSM, the phase shift angle λ is adjusted until a satisfactory solution is obtained. Solutions are, in this context, values of λ where, at field current corresponding to leading, unity, and lagging power factor, the machine is operating at rated torque. The torque is known because the active output power is 80.8kW for all operating points. Furthermore, the 2D VSM is also required to give rated voltage at all operating points.

The approach is initiated by performing a parametric sweep for the angle λ. The angle is varied from an arbitrary starting angle to a predefined stop angle. A time-dependent study is carried out for each point. The initial rotor angle is fixed, and the rotor is given the rated angular speed. Once satisfactory solutions for λ are obtained, the angle λ is fixed. Obtained values for λ are then implemented in the 3D VSM model, thus completing the analysis.

The 2D VSM is highly beneficial for conducting this analysis. If the analysis is carried out on the 3D VSM, significant computational power is needed, and the simulation time would by far exceed the time frame of this thesis. Furthermore, time-dependent studies on the 3D model are not necessarily beneficial as an implementation of torque calculations in 3D requires fine mesh, thus further increasing the simulation time.

3.1.5 Materials

The stator iron is made of non-oriented electrical steel grade M400-50A. The material properties of the stator iron material are experimentally obtained and investigated in the work preceding this thesis. The magnetic properties of the stator iron material are investigated for compressive stress in the stacking direction in the specialization project Fagermyr [6]. An experimental investigation is completed to obtain an improved B-H curve that can be implemented in modeling the VSM stator core. In addition to a brief test setup description, relevant conclusions from Fagermyr [6] are included in this thesis. Complementary details are available in [6].

The effect of continuous compressive stress on the magnetic properties of non-oriented electrical steel is investigated to determine the possible effect of stacking pressure in the stator core. Traditional measurement techniques like the Epstein frame are unsuitable for applying pressure in the stacking direction. A small ring core is made using laminated non-oriented electrical steel grade M400-50A cut specifically for this purpose. In the stacking direction, the ring core is tested at a compressive stress of 0MPa, 5Mpa, and 10MPa. At each level of compressive stress, the magnetic properties are investigated for selected frequencies.

The fully wound ring core is shown in Figure 3.12(a). Figure 3.12(b) shows the ring core with external pressure applied in the stacking direction using a hydraulic press.

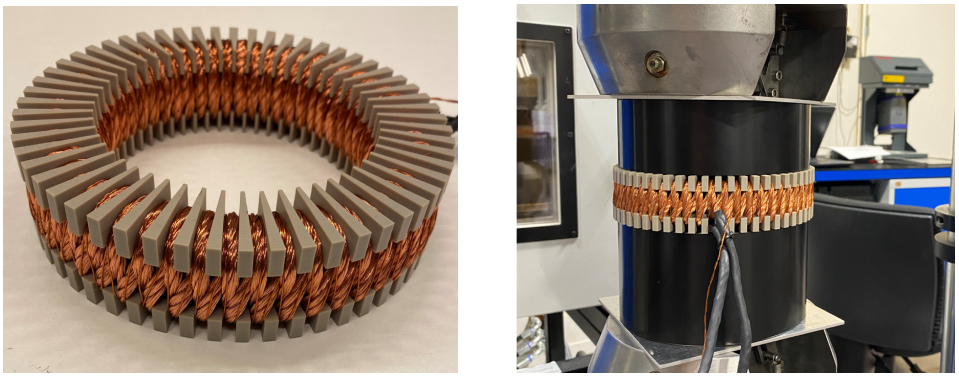

(a) **(b)**

Figure 3.12. Fully wound ring core: (a) with winding slots visible and no external pressure; (b) with mechanical stress included.

In Fagermyr [6] the magnetic properties of M400-50A are investigated for excitation frequencies in the range of 50Hz-1kHz for compressive stress of 0MPa - 10MPa. Results show that increasing stress in the stacking direction reduces the permeability of the iron. The difference is most prominent in the B-H curve knee point. Indeed, evaluated at magnetic field strength H of 200A/m, the magnetic flux density B is reduced by 8.9 % and 15.5% relative to the no pressure base case for 5MPa and 10MPa respectively [6]. The experimentally obtained BH-curve at 50Hz excitation used in modeling the VSM is presented in Figure 3.13.

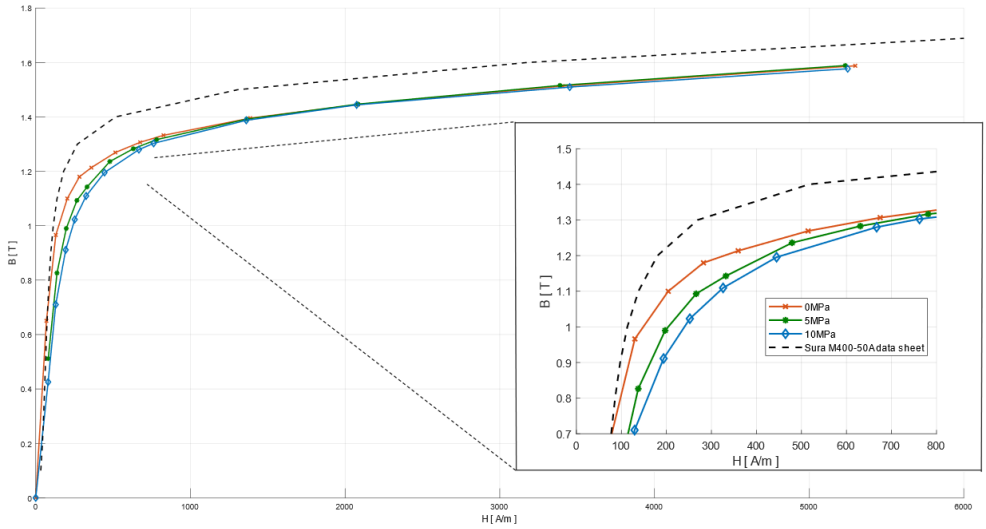

Figure 3.13. BH-curves for increasing mechanical stress with 50Hz excitation current from Fagermyr [6].

As described in section 2.3, the relative permeability of the stator iron is not uniform. Instead, the relative permeability is generally high in the plan of laminated sheets, and low in the direction normal to the main flux. In the model, this characteristic can be imitated by modeling each sheet individually, with domains of low permeability separating sheets. However, such implementation is not preferable as it further complicates the model geometry and meshing. Instead, the anisotropic characteristics of laminated electrical steel is implemented directly in the model. The implementation is achieved by specifying anisotropic relative permeability in the $\hat{x}$, $\hat{y}$ and $\hat{z}$ direction as shown in Equation 3.1.2.

$$\mu_r = \begin{bmatrix} k_s\mu_r|_{B_x} & 0 & 0 \\ 0 & k_s\mu_r|_{B_y} & 0 \\ 0 & 0 & 20 \end{bmatrix} \tag{3.1.2}$$

In Equation 3.1.2, $\mu_r|_{B_x}$ is the relative permeability evaluated at the magnetic flux density x-component B_x, and $\mu_r|_{B_y}$ is the relative permeability evaluated at the magnetic flux density y-component B_y. With this implementation, the relative permeability of the stator iron depends of the saturation level. The permeability curve is created using the B-H curve obtained in work preceding this thesis Fagermyr [6], and the curve is included in A.3. The stacking factor is k_s is 0.95.

A similar approach is used to define the stator iron's electrical conductivity. The conductivity is found in the corresponding data sheet in the plane of sheets. According to the Sura data sheet A.7, the electrical resistivity is 42 $\mu\Omega cm$, corresponding to electrical conductivity of $\sigma_x = \sigma_y = 2.381$ MS/m. The electrical conductivity is thus implemented as shown in Equation 3.1.3 for the stator iron.

$$\sigma = \begin{bmatrix} k_s\sigma_x & 0 & 0 \\ 0 & k_s\sigma_y & 0 \\ 0 & 0 & 0 \end{bmatrix} \tag{3.1.3}$$

3.1.6 Validation of the generator 3D model

The generator 3D model simplifies the real generator design with the number of slots changed from 114 to 126, as emphasized in section 3.1. Consequently, there are geometrical differences between the 3D integral slot VSM model and the fractional slot RSM model, as well as electrical differences. Direct comparison between the 3D VSM model and data sheet test results is not considered relevant. To verify that the 3D sector model is correctly implemented, a simplified 3D model is used. The simplified 3D model is created from the 3D VSM model with the stator end windings and the end region field winding removed. The simplified 3D VSM is presented in Figure 3.14.

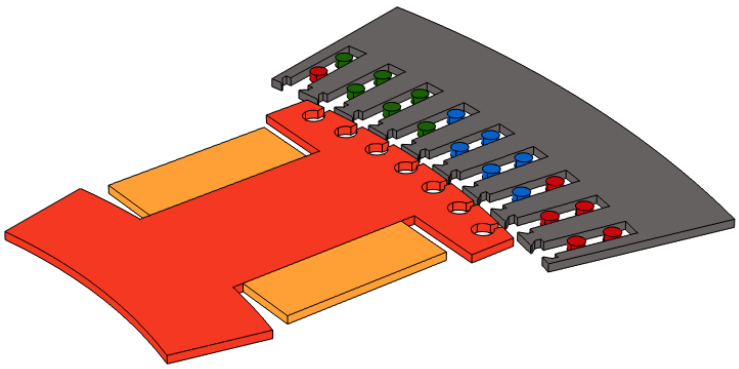

Figure 3.14. Simplified 3D VSM geometry. Air domains are hidden.

For validation of the 3D model implementation, the radial component of the airgap flux density is evaluated under no-load conditions with field current as defined in the operating points from Table V. The airgap flux density is evaluated in the airgap along the boundary line, separating the rotating and stationary domains for the 2D VSM and the simplified 3D VSM.

The end region is special considering the field from the end windings in loaded operation and the rotor field winding end-part. The simplified 3D model without all of the end windings and pressing structures is thus used to ensure that the results can be comparable to the 2D model, with both no-load and loaded tests. Due to the armature reaction and significant field from the end winding under loaded operation, a direct comparison between the 3D VSM and the 2D model is not considered. As the simplified 3D model is more representative of an arbitrary generator cross-section and is thus comparable to the 2D VSM model. Further validation of the 3D model is conducted by inspection of the no-load induced voltage. A comparison is made for the 2D VSM no-load test curve and the 3D-model no-load test points corresponding to the operation points from Table V.

3.2 Artificial leakage flux laboratory test

A loss measurement apparatus is constructed for investigating the effect of leakage flux is presented in this section. The complete test setup consists of an Epstein frame and a C-shaped core with suitable measuring and monitoring. The measurement apparatus is based on the procedure proposed in [12]. First, the Epstein frame is described in section 3.2.1. Secondly, the C-shaped core for introducing magnetic flux normal to the main flux is described in section 3.2.2. Finally, the complete test configuration with Epstein frame and C-shaped is presented in section 3.2.4. The measuring equipment and the excitation system are briefly described in section 3.2.3, derived from the work preceding this thesis Fagermyr [6]. A developed FEM model of the real test setup is described in section 3.2.5.

3.2.1 Epstein frame

The Epstein frame is a commonly used measurement system for obtaining material properties. The Epstein frame consists of three main parts; a laminated iron core, a primary winding, and a secondary winding. The iron core consists of electrical sheets assembled in a square, thus forming a closed magnetic circuit. The primary winding is used to set up the magnetic flux in the core. The secondary winding is used to measure the induced voltage. The iron core losses are calculated by measuring the excitation current in the primary winding and the induced voltage in the secondary winding. A simplified schematic representation of the Epstein frame setup is presented in Figure 3.15(a). A 2D representation of the actual test setup is illustrated in Figure 3.15(b).

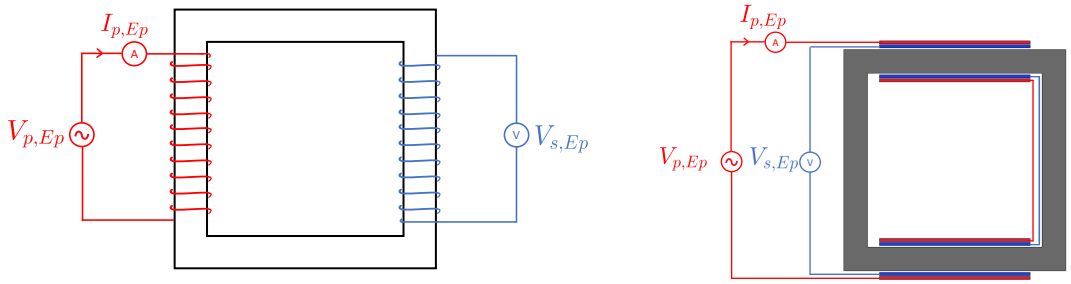

(a) **(b)**

Figure 3.15. Epstein frame setup with primary side winding in red and secondary side winding in blue. $V_{p,Ep}$ = primary side supply voltage, $V_{s,Ep}$ = induced secondary side voltage, $I_{p,Ep}$ = primary side excitation current. Illustrations of: (a) schematic illustration of the Epstein frame; (b) realistic cross-sectional representation of the Epstein frame test setup.

The working principle of the Epstein Frame is similar to that of a transformer. A supply voltage $V_{p,Ep}$ is applied across the excitation winding terminals on the primary side, as illustrated in Figure 3.15(a). The primary side current $I_{p,Ep}$ is the magnetizing current since the circuit works as a transformer under no-load operating conditions. The magnetic field strength associated with the measured excitation current is obtained using Equation 2.4.3.

The current in the secondary winding is assumed to be negligible considering the high internal impedance of the voltage measuring equipment. The secondary winding is referred to as the voltage pick-up winding. The voltage reading $V_{s,Ep}$ on the secondary side is used for obtaining the magnetic flux density using Equation 2.4.6.

As illustrated in Figure 3.15(b), the Epstein frame test setup uses concentric windings with the primary winding wound on top of the secondary winding. The windings are

placed on two opposite sides and connected in series as illustrated in figure Figure 3.15(b).

The Epstein frame apparatus is assembled following the procedure introduced in [12] and the frame is very similar in design. Indeed, the Epstein frame windings and the aluminum support plate are from [12]. The key difference regarding the Epstein frame setup is the choice of electrical steel and the method used for assembling sheets. Geometrical properties and selected parameters from the Epstein frame setup are given in Table VI.

TABLE VI. Epstein frame apparatus parameters

Description	Value	Unit
Frame inner width	220	$[mm]$
Frame outer width	280	$[mm]$
Sheets thickness	0.35	$[mm]$
Sheets width	30	$[mm]$
Number of sheets	86×4	[-]
Primary coil diameter	2.0	$[mm]$
Secondary coil diameter	1.0	$[mm]$
Number of turns excitation winding	200	[-]
Number of turns secondary winding	200	[-]

In the Epstein frame's single flux test (SFT), the primary winding is excited using an external power source. The flux in the iron core is thus only affected by the single source excitation provided by the single-phase power supply. The purpose of the Epstein frame SFT is to investigate the material properties of the iron core under single source excitation. The relationship between magnetic field strength and resulting magnetic flux density is obtained. Furthermore, the Epstein frame's watt-meter characteristics provide insight into the iron core power loss for a selected range of excitation current magnitudes. For the SFT, the complete Epstein frame set up shown in Figure 3.16 in accordance with the schematic representation in Figure 3.15(b).

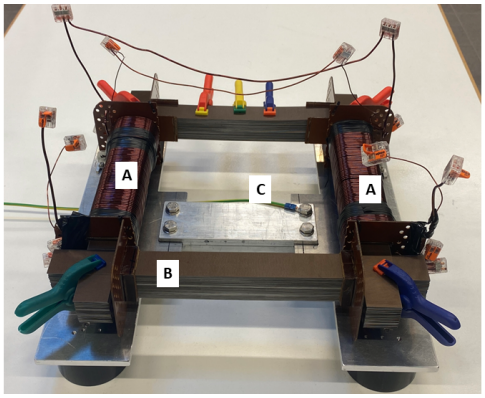

Figure 3.16. The Epstein frame apparatus with A: primary and secondary winding, B: iron core, C: grounding of aluminium support plate

Plastic pressure clamps ensure a satisfactory rigid construction. In Figure 3.16, the pressure clamps on the front-facing side are removed for the benefit of visualization.

3.2.2 C-core

The C-core is a C-shaped iron core with separate excitation. The main purpose of the C-core is to introduce a magnetic field normal to the main core rolling direction. Similar to the Epstein frame excitation arrangement, the C-core assembly consists of a primary excitation winding, a secondary winding for measuring the induced voltage, and an iron core. A schematic illustration of the C-core is presented in Figure 3.17.

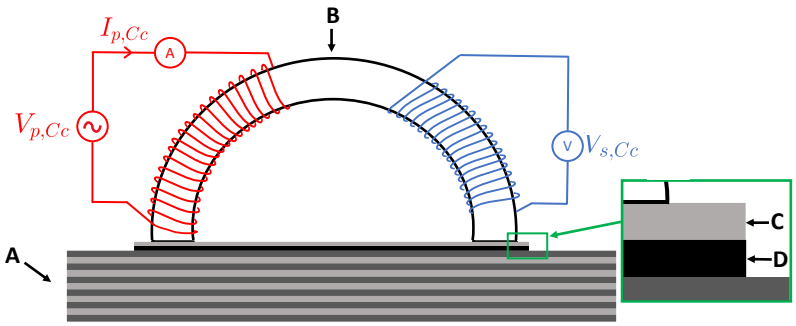

Figure 3.17. Schematic illustration of the C-core. A: Epstein frame iron core, B: C-core iron, C: PTFE plate, D: Steel plate. Illustration inspired by [12]. $V_{p,Cc}$ = C-core primary side supply voltage, $V_{s,Cc}$ = C-core secondary induced voltage, $I_{p,Cc}$ = primary winding excitation current

A PTFE plate is placed in the airgap between the Epstein frame iron and the C-core to provide magnetic insulation and to ensure uniform airgap length. A plate of stainless steel 316L is also placed in the airgap, illustrated in Figure 3.17. The purpose of the steel plate is to emulate the pressing structures in the end region of a synchronous generator. The C-core flux return path is in the Epstein frame iron core and steel plate. With the implementation of the PTFE plate and the steel plate in the airgap constituting high reluctance elements, the magnetic flux density is dramatically reduced in the C-core magnetic circuit.

In Figure 3.17, the primary and secondary winding are mounted on opposite sides of the core. However, in constructing the C-core, the primary winding is wound on top of the secondary winding, following the design proposed in [12]. Separating the windings from the iron is a support jig ensuring minimal mechanical strain on the winding insulation and improving the overall rigidity of the construction. The construction process is presented in Figure 3.18.

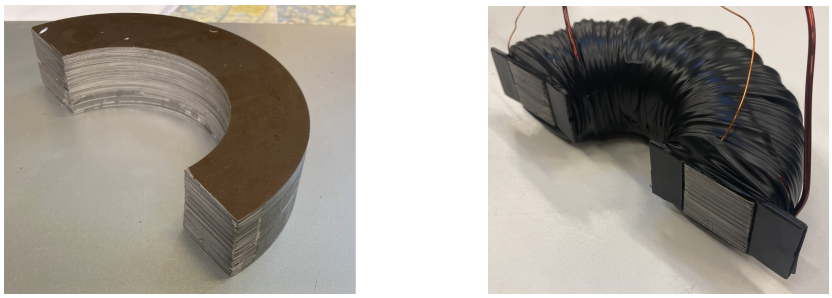

(a) **(b)**

Figure 3.18. The C-core building process with: (a) Laminated electrical steel core; (b) Complete C-core with primary excitation winding, secondary voltage pickup winding and support jig.

The design parameters for the C-core dimensions and parameters of interest is presented in Table VII.

TABLE VII. C-core parameters

Description	Value	Unit
Primary winding diameter	0.9	$[mm]$
Secondary winding diameter	0.5	$[mm]$
Sheet thickness	0.35	$[mm]$
Number of sheets	73	[-]
Core inner diameter	77	$[mm]$
Core outer diameter	132	$[mm]$
Number of turns excitation winding	200	[-]
Number of turns pick up winding	200	[-]

In the C-core single flux test, an excitation voltage $V_{p,Cc}$ is applied across the C-core excitation windings terminals as illustrated in Figure 3.17. The main field from the Epstein frame winding is not excited in the C-core SFT. The induced voltage in C-core secondary winding is measured for increasing excitation voltage. With the watt-meter characteristics of the C-core circuit, power losses are measured for increasing excitation voltage.

From the C-core SFT, the measured excitation current and the induced voltage are used to form a B-H curve. The C-core circuit is unsuitable for investigating the core material properties due to the magnetic insulation and steel plate. However, the B-H curve is used to obtain the appropriate excitation voltage for the desired magnetic flux density in the C-core. Additionally, the C-core SFT obtained power loss is used as a reference in the artificial leakage flux test described in section 3.2.4.

3.2.3 Excitation and measuring system

The complete test setup consists of a three-phase power supply, a power analyzer, an IR camera, and the Epstein frame and C-core. The complete test setup is shown in Figure 3.19.

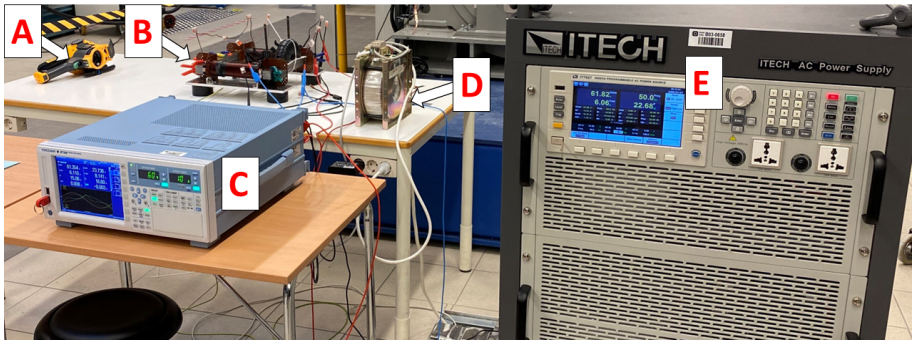

Figure 3.19. The complete test setup with: A: IR camera, B: Epstein frame and C-Core, C: Power Analyzer, D: Insulation transformer, E: Three phase Power Supply

The ITECH programmable AC power supply (IT7627) provides excitation current to the Epstein frame and the C-core. The power supply is used in the unbalanced mode, where one output phase is used for the Epstein frame and a second output phase is used for the C-core. The third output phase is not used. The voltage magnitude of each output phase can be adjusted separately from the control panel. Additionally, the phase shift between output phases is adjustable in the unbalanced operating mode.

The WT1800 Precision Power Analyzer is used to monitor excitation currents and induced voltages. Current and voltage waveforms are obtained and stored using the data acquisition capability of the power analyzer. The WT1800 Precision Power Analyzer guarantees voltage measurement accuracy with an error of minimum ±(0.1% reading + 0.1% range) for measurements with frequency 45Hz< f <1kHZ. The error of the current measurements is ±(0.2% reading + 0.1% range) for the same frequency range. The maximum error relative to the measured voltage is ±0.4%, and the maximum error relative to the measured current is ± = 0.7%, which are considered acceptable. An IR camera is used for the measurement of steel temperature.

3.2.4 Artificial leakage flux test setup

The ALF test is a combination of the single flux tests described for the Epstein frame in section 3.2.1 and the C-core in section 3.2.2. The ALF test investigates how power losses are affected by the external magnetic flux provided by the C-core, emulating the leakage flux in the end region of a synchronous generator. Furthermore, it is of particular interest to observe how measured losses are affected by changing the angle between the Epstein frame main flux and the external flux from the C-core. The ALF test is repeated with steel plates of varying thickness placed in the airgap.

In the ALF test, the Epstein frame and C-core are magnetized simultaneously. The placement of the C-core relative to the Epstein frame in the ALF test is illustrated in Figure 3.20, following the placement of the C-core described in section 3.2.2.

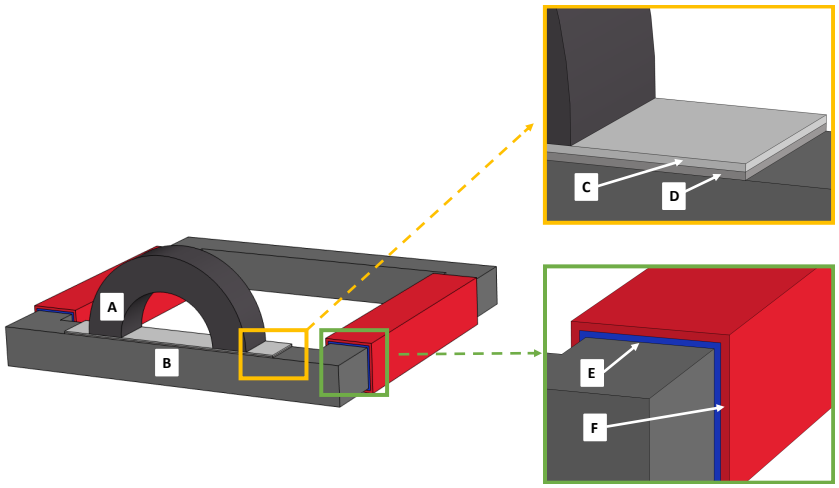

Figure 3.20. CAD model of the test setup. C-core windings are not included. A: C-core, B: Epstein frame core, C: Magnetic insulation (PTFE plate), D: Steel plate, E: Epstein frame secondary winding, F: Epstein frame primary winding

The model in Figure 3.20 is used for FEM-modelling of the ALF test and SFT of the Epstein frame and C-core. The FEM model is described in section 3.2.5. A schematic representation of the ALF test setup is presented in Figure 3.21, with the power supply operating in unbalanced mode, as described in section 3.2.3.

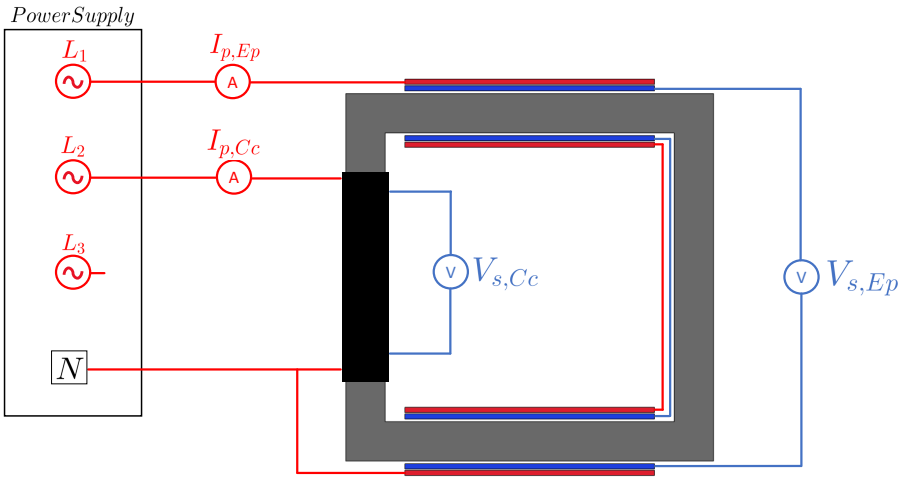

Figure 3.21. Schematic drawing artificial leakage flux test. $I_{p,Ep}$ = Epstein frame excitation current, $I_{p,Cc}$ = C-core excitation current, $V_{s,Cc}$ = C-core induced voltage, $V_{s,Ep}$ = Epstein frame induced voltage, L_1, L_2, L_3 = Power supply output phases, N = Power supply neutral.

Initial investigation of the magnetic flux density at different excitation current levels is required for the Epstein frame and the C-core to obtain the operation point at the desired flux density. The desired flux density in the Epstein frame core is 1.5T. For the C-core, the desired flux density is 0.8T.

For single excitation of the Epstein frame and the C-core, the magnetic flux density in the iron core is calculated using the induced voltage measured in the secondary winding following the relationship in Equation 2.4.6 for each core respectively. Hysteresis loops at each excitation level are formed by combining Equation 2.4.6 and Equation 2.4.3. Finally, the BH-curve is created using the procedure presented in subsection 2.4.2, where the

BH-loop tip points are combined to form the BH-curve.

Physical implementation of the ALF test

The ALF test goal is to investigate how core losses are affected by a separate magnetic field interfering with the main field at different phase angles. The incremental losses is the difference between the ALF test losses and the sum of losses under single excitation. Consequently, the incremental losses are a direct measure of the impact of introducing a magnetic field in the normal direction. The ALF test uses the following procedure to obtain the power losses under different voltage phase shift angles and varying steel plate thickness.

ALF test procedure

1. **Epstein frame**

   1.1. Identification of the excitation voltage corresponding to desired flux density in the Epstein frame core by inspecting the experimentally obtained B-H curve. The selected flux density B_m in the Epstein frame core is 1.5T.

   1.2. Measurement of reference losses for Epstein frame at magnetic flux density of $B_m = 1.5$T.

2. **C-core**

   2.1. Identification of the excitation voltage corresponding to desired flux density in the C-core by inspection of the experimentally obtained BH-curve. The selected flux density B_m in the C-core is 0.8T.

   2.2. Measurement of reference losses for the C-core at a magnetic flux density of $B_m = 0.8$T.

3. **ALF test**

   3.1. Conducting the artificial leakage flux test (ALF test). Compare the total losses to the single flux test losses in points 1.2 and point 2.2. Incremental losses are obtained.

   3.2. The ALF test is repeated for phase shift of 30°, 60°, 90°, 120°, 150° and 180°.

   3.3. The ALF test is repeated with 1mm steel plate and 2mm steel plate at all voltage phase angles in point 3.2.

Operating points for the ALF test are found using the experimentally obtained B-H curve for the Epstein frame core evaluated at a magnetic flux density of 1.5T and the B-H curve evaluated at 0.8T in A.6. The resulting excitation voltage corresponding to the desired flux density is 61.25V and 23.89V for the Epstein frame and C-core, respectively.

3.2.5 FEM model of the test set up

A 3D model of the test setup is created to visualize the magnetic flux density in the Epstein frame core and the C-core. The model geometry is shown in Figure 3.20. The excitation winding of the Epstein frame and the C-core is modeled using the inbuilt multiturn coil under the assumption of uniform current density distribution in the excitation winding. In the construction of the C-core in Figure 3.18 and Epstein frame windings from [12], the winding turns are uniformly distributed in the winding. Consequently, the assumption of uniform current distribution in the FEM model is considered acceptable.

Anisotropic magnetic permeability is implemented in the Epstein frame iron core using the M300-35A data sheet BH-curve from A.5. Electrical conductivity of the stainless steel plate is $\sigma = 1.33[MS/m]$. The magnetic insulation plate is assigned the material properties of air. A time-dependent study is performed over one 50Hz electrical period. Several tests are performed on the FEM model to support the laboratory tests.

First, single flux tests (SFT) are conducted on the Epstein frame model and the C-core model to observe magnetic flux density distribution. Excitation current for the Epstein frame and C-core is found using the SFT results. FEM model single flux test results are referred to as FEM-SFT results.

Secondly, artificial leakage flux tests are performed on the FEM model with unchanged excitation current magnitude from the SFT. The phase shift angle θ between the applied excitation voltages on the Epstein frame and C-core windings is assumed to cause an equal phase shift between excitation currents. With the Epstein frame excitation current as a reference, the C-core excitation current lags an angle θ. The FEM-ALF test is simulated at $\theta = 0°$, $\theta = 90°$ and $\theta = 180°$. The excitation current used in the FEM-ALF test is presented in Figure 3.22.

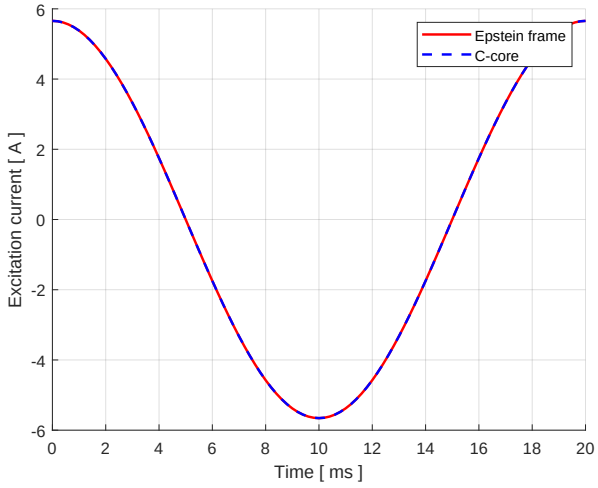

(a)

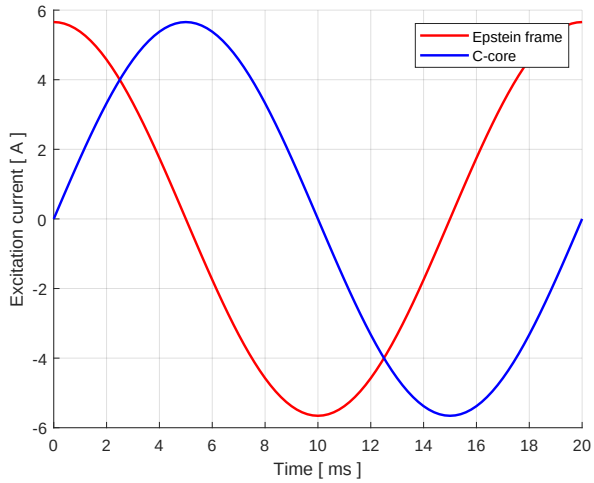

(b)

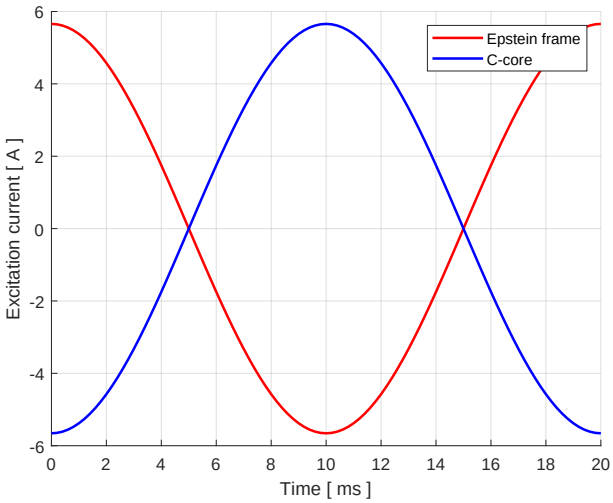

(c)

Figure 3.22. Epstein frame and C-core currents used in the FEM-ALF test for phase shift angle θ of: (a) 0°; (b) 90°; (c) 180°.

Chapter 4

Results

The results presented in this thesis are sectioned into two main parts. Simulation results on the 2D and 3D FEM models of the synchronous generator are presented in section 4.1. Results from the laboratory test of artificial leakage flux are presented in section 4.2.

4.1 Synchronous Generator Modelling

The results obtained from the 2D VSM model and 3D VSM model are presented in this section. First, the simplified 3D model test results are compared to the 2D model test results in section 4.1.1 to validate that the 3D model is correctly implemented. Secondly, the simulation results of the complete 3D model under varying loading are presented in section 4.1.2, including an evaluation of the end region losses.

4.1.1 Validation of the 3D VSM model

The simplified 3D VSM model is used to validate the complete VSM model by comparing several test results with the 2D VSM model, as described in section 3.1.6. The first is a no-load test with field current equal to the operating points in Table V. The results obtained in this analysis are presented here. The magnetic flux density norm from the no-load test is presented in Figure 4.1(a) and Figure 4.1(b) for the 2D VSM model and 3D simplified VSM respectively.

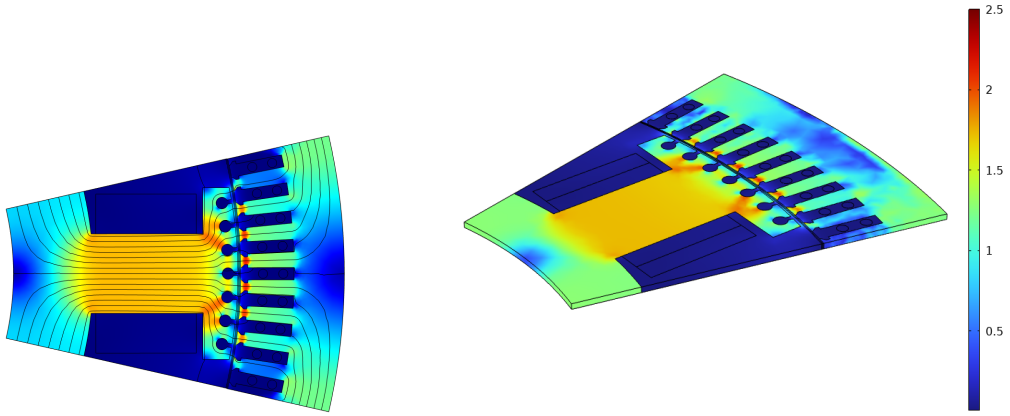

(a) **(b)**

Figure 4.1. No load test magnetic flux density norm with a range up to 2.5T. Field current corresponding to unity power factor. Results from: (a) 2D VSM model; 3D simplified VSM model.

Only minor differences between the magnetic flux density norm of the 2D model and the simplified 3D model can be observed. Overall, the 3D VSM produces a similar no-load flux density in the rotor iron and stator iron as in the 2D model for identical field current. For further validation of the implementation of the 3D VSM model, the induced no-load voltage is compared. Resulting no-load voltages for the simplified 3D VSM model is presented in Figure 4.2(a), Figure 4.2(b) and Figure 4.2(c) with field current corresponding to leading power factor, unity power factor and lagging power factor respectively.

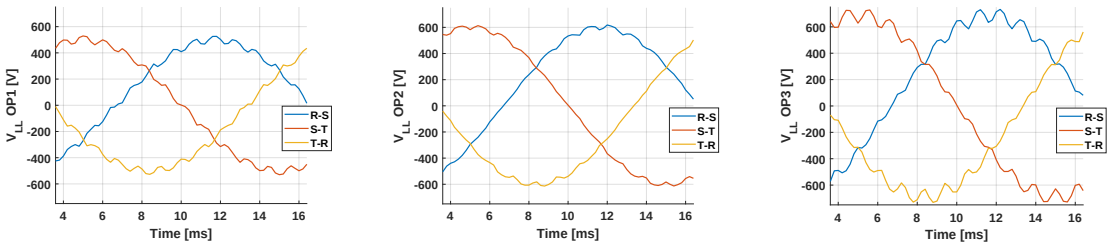

(a) **(b)** **(c)**

Figure 4.2. Simulated no-load tests on the simplified VSM with the field current corresponding to: (a) Leading power factor; (b) Unity power factor; (c) Lagging power factor.

For comparison, the induced no-load voltage for the 2D VSM model is presented at leading power factor in Figure 4.3(a), at unity power factor in Figure 4.3(b) and at lagging power factor in Figure 4.3(c).

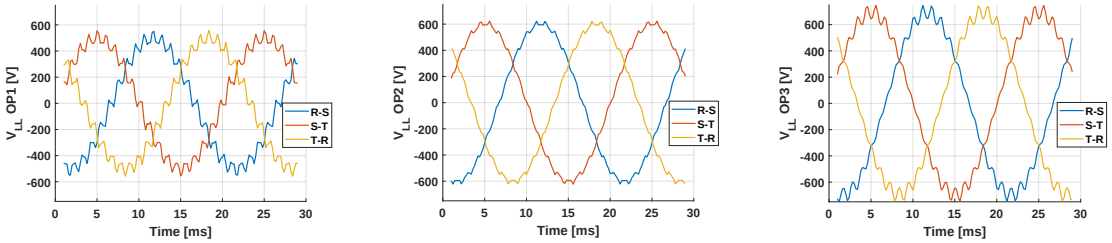

(a) **(b)** **(c)**

Figure 4.3. Simulated no-load tests on the 2D VSM with the field current corresponding to: (a) Leading power factor; (b) Unity power factor; (c) Lagging power factor.

Only small differences exist between the induced no-load voltages in the 2D model and the simplified 2D VSM model. As expected, the magnitude of no-load voltages is increasing for increased field current. In Figure 4.3(c) and Figure 4.2(c), the voltage magnitude exceeds the rated RMS voltage of 400V, as field current is higher than the associated rated current.

The final comparison in the no-load test is an investigation of the radial component of the magnetic flux density in the airgap, as described in section 3.1.6. Figure 4.4 shows the airgap magnetic flux density evaluated in the boundary separating the rotating and stationary domains at a selected time step.

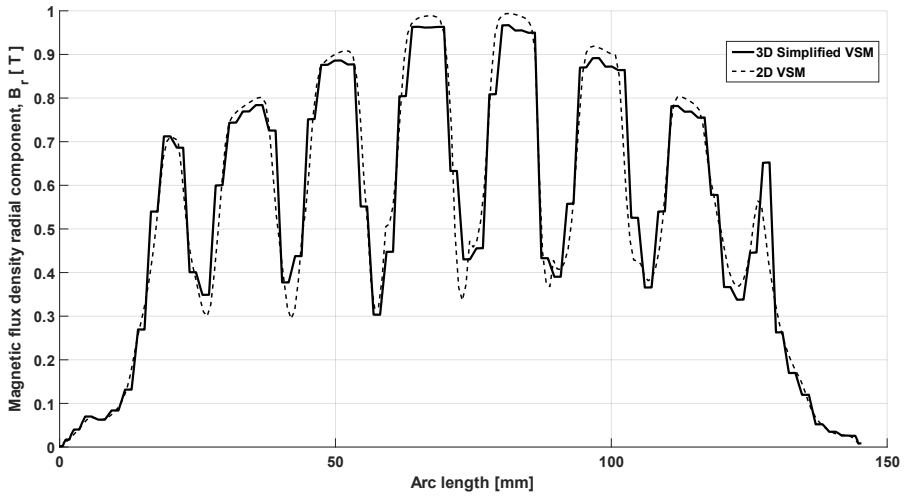

Figure 4.4. Magnetic flux density radial component evaluated in the airgap under no-load test for the 2D VSM and simplified 3D VSM model.

The flux density in Figure 4.4 is obtained in the no-load test with field current corresponding to unity power factor. Comparisons are also made at leading and lagging power factor, showing only minor differences similar to the airgap flux density in Figure 4.4.

Similar to the no-load test procedure, a comparison is made between the magnetic flux density of the 2D model and the simplified 3D VSM model at unity power factor. The magnetic flux density norm is shown in Figure 4.5(a) for the 2D model and in Figure 4.5(b) for the simplified 3D VSM model.

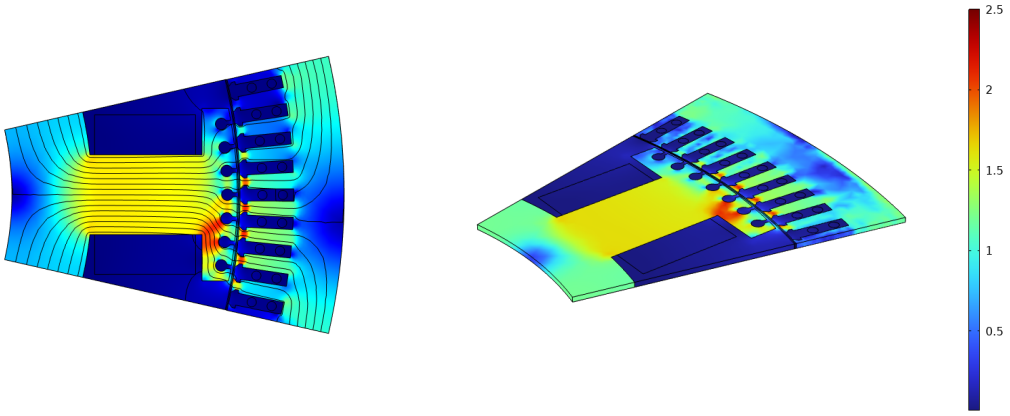

(a) **(b)**

Figure 4.5. Loaded test at unity power factor for comparison of magnetic flux density norm with a range up to 2.5T. Results from: (a) 2D VSM model; 3D simplified VSM model.

Apart from some differences in the flux density in the rotor yoke, the flux density in the simplified 3D VSM model is equal to the 2D VSM model under loaded operation at unity power factor. Under identical conditions as in Figure 4.5, the airgap magnetic flux density radial component is investigated along a selected airgap boundary line. The resulting flux density plot is shown in Figure 4.6.

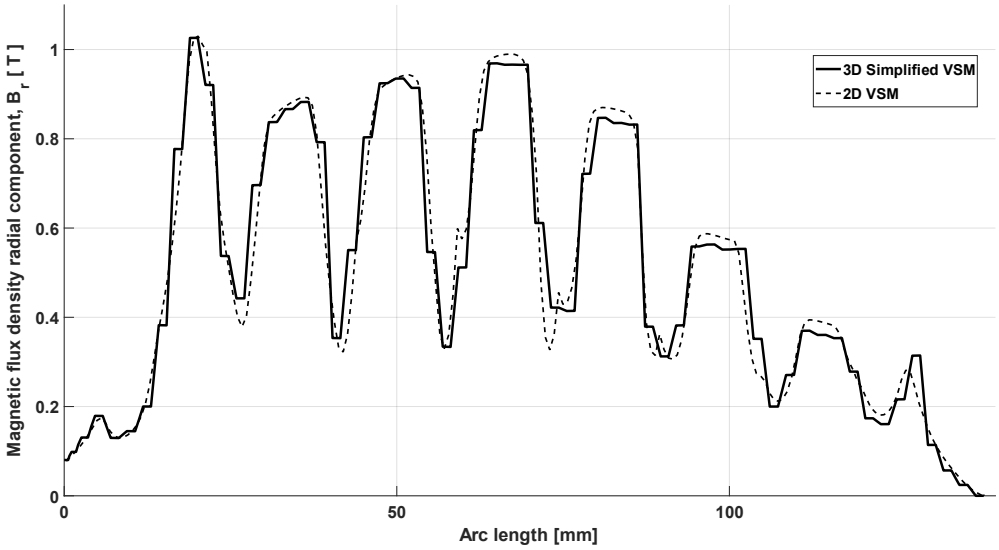

Figure 4.6. Magnetic flux density radial component evaluated in the airgap at unity power factor for the 2D VSM and simplified 3D VSM model.

The magnetic flux density in the airgap under loaded conditions is shifted to the side as expected. The tendency is also observable in Figure 4.5 for both the 2D and 3D model. Similar to the no-load test airgap flux density, the airgap flux under loaded conditions is nearly identical.

4.1.2 Complete 3D VSM model results

From the analysis in section 3.1.6 it is concluded that the 3D model is correctly implemented, and the complete 3D VSM model can thus be used in further analysis.

Further evaluation of end region losses is based on loaded simulations of the complete 3D VSM with varying power factor. Using the 3D VSM model, the magnetic flux density is investigated for selected operating points in the end region pressing structure and stator iron. The operating points are leading power factor, unity power factor, and lagging power factor, from Table V. The magnetic flux density norm is presented in Figure 4.7-4.9 in the end region clamping plate, press fingers and stator iron. For improved visibility of the relevant domains, the complete geometry is expanded into three separate parts indicated by letters a, b and c in Figure 4.7-4.9.

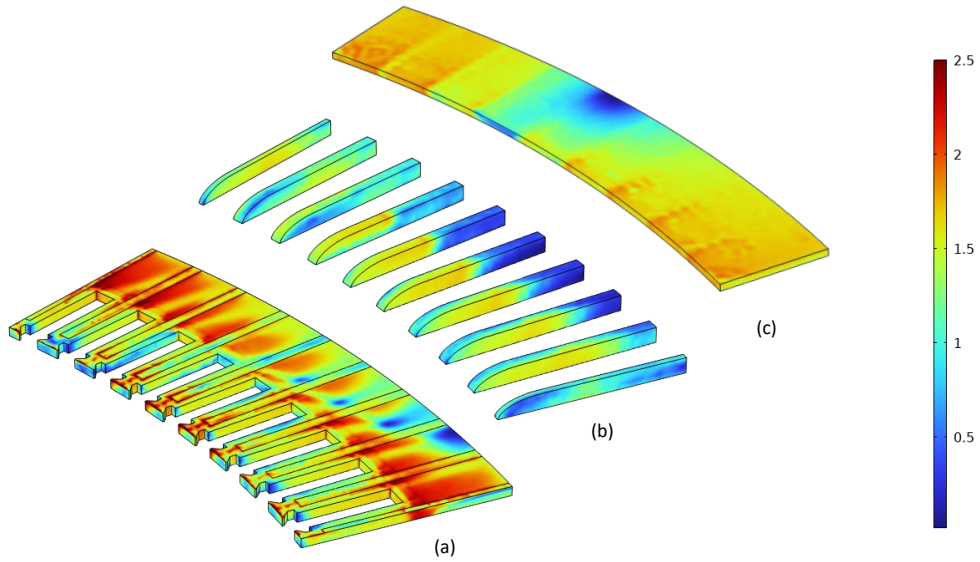

Figure 4.7. Magnetic flux density norm with range of 0-2.5T at leading power factor in the end region: (a) stator iron; (b) press fingers; (c) clamping plate.

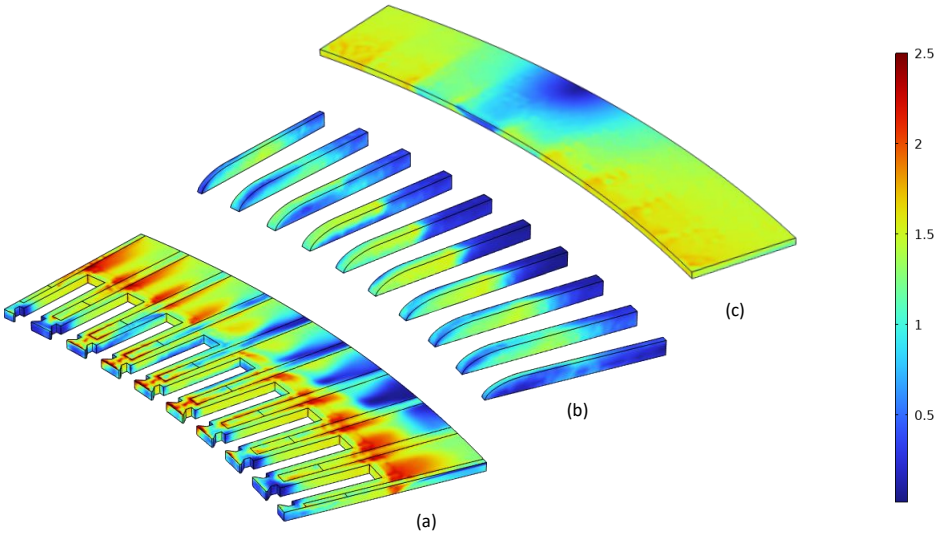

Figure 4.8. Magnetic flux density norm with range of 0-2.5T at unity power factor in the end region: (a) stator iron; (b) press fingers; (c) clamping plate.

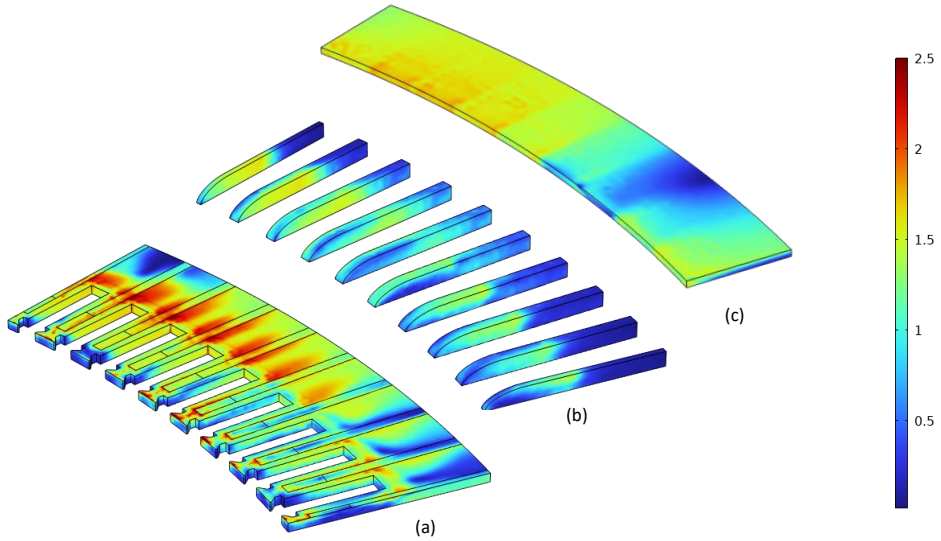

Figure 4.9. Magnetic flux density norm with range of 0-2.5T at lagging power factor in the end region: (a) stator iron; (b) press fingers; (c) clamping plate.

The magnetic flux density norm is significantly higher when the generator works under leading power factor conditions by visual inspection of the obtained magnetic flux density norm in Figure 4.7-4.9. A similar trend is observable for the press fingers and clamping plate when comparing the leading power factor case to the unity and lagging power factor situation. The difference in magnetic flux density at unity power factor and leading power factor is negligible.

The magnetic flux in the generator end region consists of a considerable axial component, the effect of which is of particular interest for the investigation of the end region losses. The axial component of the end region magnetic flux is investigated for leading power factor, unity power factor, and leading power factor. Results obtained in the pressing fingers are presented in Figure 4.10. Results for the stator iron is presented in Figure 4.11.

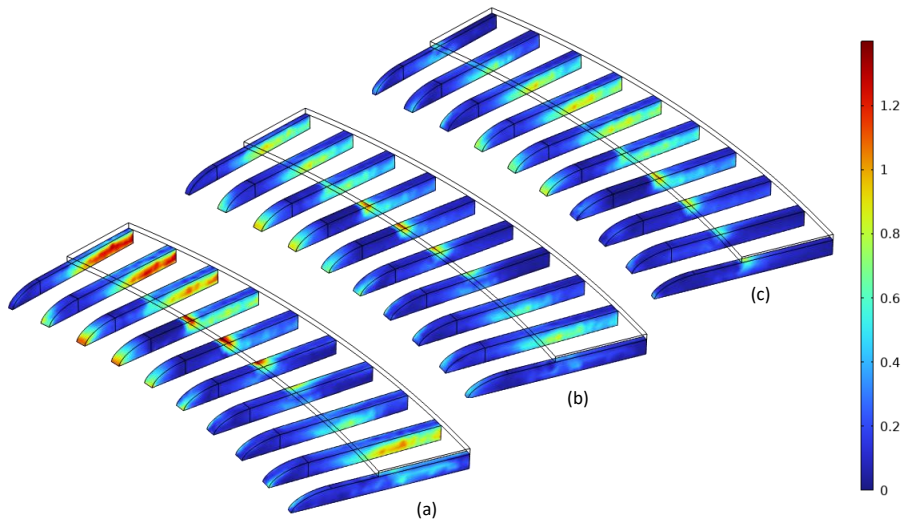

Figure 4.10. Magnetic flux axial component B_z plot of the end region press fingers. The clamping plate is hidden. B_z on a scale of 0-1.3T at: (a) leading power factor; (b) unity power factor; (c) lagging power factor.

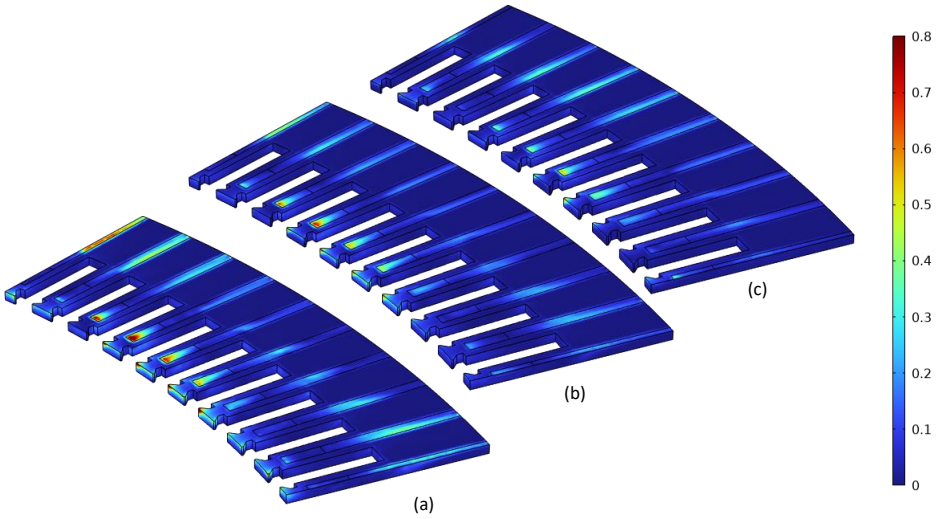

Figure 4.11. Magnetic flux axial component B_z plot of the end region stator iron. The clamping plate and press fingers are hidden. B_z on a scale of 0-0.8T at: (a) leading power factor; (b) unity power factor; (c) lagging power factor.

The axial component of the magnetic flux density B_z is significantly higher in the under-excited operating point when evaluated in the press fingers in Figure 4.10. The difference is most significant in the press fingers directly underneath the clamping plate. In general, the radial component of the magnetic flux density is observably higher in the press fingers tip point than in the press finger middle part. The difference between operation points is less significant when evaluating the magnetic flux density axial component B_z in the stator iron in Figure 4.11. It is also worth noting that the scale on which B_z plotted is lower in Figure 4.11 than in Figure 4.10.

The eddy currents induced in the generator end region pressing structure are investigated by evaluating the current density in the clamping plate and the press fingers at each of the selected operating points. Figure 4.12 shows the current density plot for the clamping plate and press fingers.

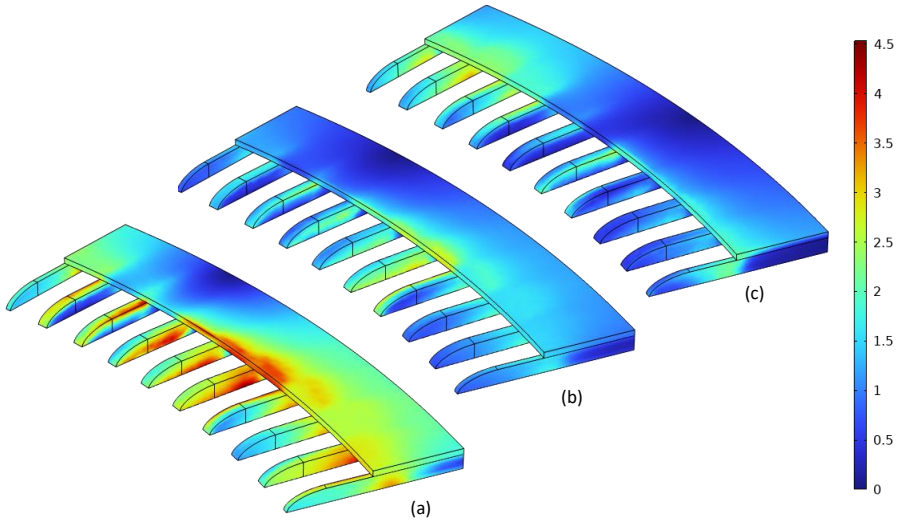

Figure 4.12. Current density in in pressing fingers and clamping plate on a scale of 0-4.5A/mm^2 at: (a) leading power factor; (b) unity power factor; (c) lagging power factor.

The current density evaluated at leading power factor in Figure 4.12(a) is observably higher than at unity power factor in Figure 4.12(b) and at lagging power factor in Figure 4.12(c). The current density in the case of unity power factor and lagging power factor is similar.

4.1.3 End region losses

Two categories of end region losses are calculated here. The first is the eddy current losses in the end region pressing structures, the clamping plate, and press fingers. Secondly, losses in the out-most part of the stator laminated iron core are calculated.

TABLE I. End region losses evaluated at selected operating points

Operating point	**Pressing structure losses [W]**	**Stator iron losses [W]**
Leading pf	1075.80	299.34
Unity pf	339.42	88.85
Lagging pf	381.53	88.16

In Table I, the cycle averaged power loss is presented for the end region pressing structure and the end region stator iron. The stator iron is evaluated for 6 sheets in Table I. The calculated average losses in Table I should be averaged over at least one electrical period, as losses vary at each time step in simulations. However, to minimize simulation time - each simulation is run to 32% of an electrical period. This simplification is acceptable, considering the small time variations of the computed losses. For the validation of this approach, one simulation lasting one electrical period is conducted. The simulation verifies the assumption of small time-dependency for the end region losses in the stator core and pressing structure.

Pressing structure losses in Table I is the sum of losses in pressing fingers and in the clamping plate. The average loss distribution within the pressing structure is presented in Table I.

TABLE II. Pressing structure average loss distribution

	Leading pf [W]	**Unity pf [W]**	**Lagging pf [W]**
Press fingers	558.61 (52%)	173.66 (51%)	188.21 (49%)
Clamping plate	517.16 (48%)	165.76 (49%)	193.32 (51%)
Combined losses	1075.80 (100%)	339.40 (100%)	381.53 (100%)

4.2 Artificial Leakage Flux Test

The results are sectioned into three parts. First, the SFT results are presented in section 4.2.1. Secondly, the results from the ALF test are presented in section 4.2.2. Finally, the FEM model results for visualization of magnetic flux density are included in section 4.2.3.

4.2.1 Single Flux Test Results

Validation of the SFT results is initiated by investigating the measured voltage and excitation current of the Epstein frame and C-core. Typical current and voltage waveforms obtained using the Power Analyzer is presented in Figure 4.13(a) for the Epstein frame SFT and for the C-core SFT in Figure 4.13(b).

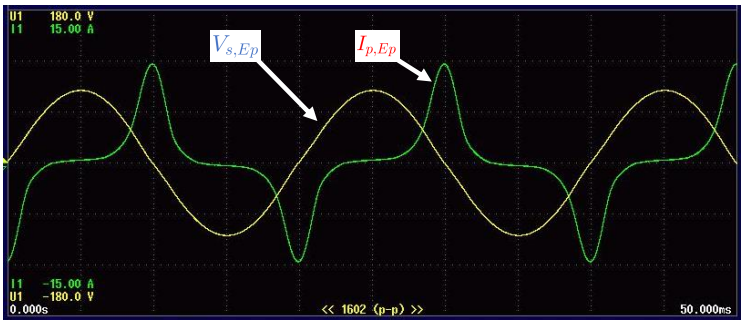

(a)

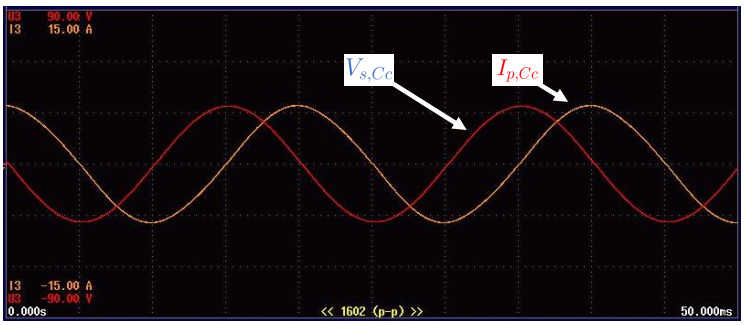

(b)

Figure 4.13. Induced voltage and excitation current waveforms obtained in the: (a) Epstein frame SFT; (b) C-core SFT.

For both single flux tests in Figure 4.13, the excitation current is lagging the voltage by approximately 90° and the measurement dc-offset is negligible. The induced voltage is sinusoidal in shape. Further validation of the test results is done by comparing the obtained B-H curve of the Epstein frame to the data sheet B-H curve for non-oriented electrical steel grade M300-35A. The procedure for creating the B-H curve, described in subsection 2.4.2, is illustrated in Figure 4.14(a). The complete experimentally obtained B-H curve for the Epstein frame iron core is presented in Figure 4.14(b) together with the M300-35A data sheet B-H curve derived from A.8.

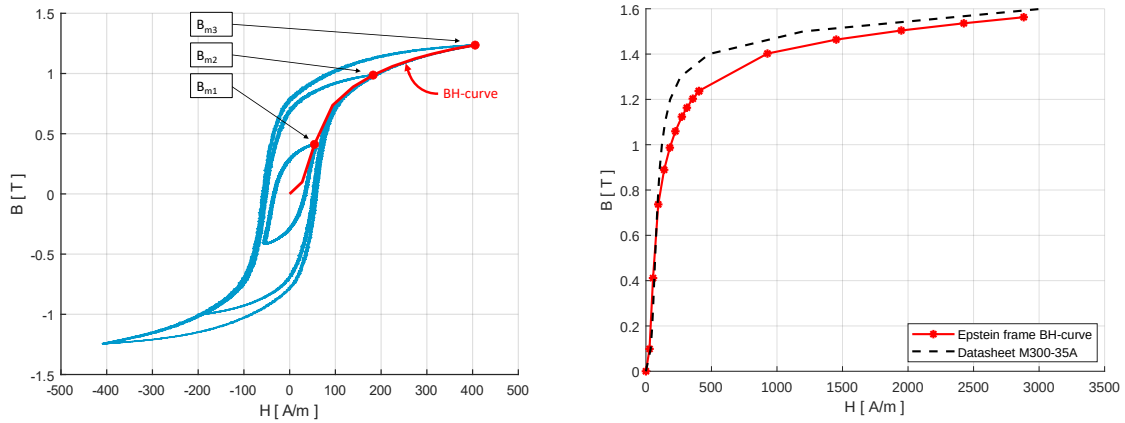

(a) **(b)**

Figure 4.14. B-H curves from the Epstein frame tests. (a) Illustration of the procedure used for obtaining the B-H curve. Selected BH-loops with at maximum magnetic flux density of B_{m1} = 0.40T, B_{m2} = 0.99T and B_{m1} = 1.24T; (b) The complete obtained B-H curve including M300-35A data sheet B-H curve.

The experimentally obtained B-H curve from the Epstein frame SFT is formed by combining tip points of 16 hysteresis loops associated with excitation current between 0.1A to 6A. For illustrative purposes, only three hysteresis curves are included in Figure 4.14(a). In Figure 4.14(b), there is a noticeable difference between the data sheet B-H curve and the experimentally obtained B-H curve. The deviation is assumed to originate from the calculation of the effective length of the Epstein frame core. Here, the effective length is calculated using the mean sheet width.

The single flux test for the Epstein Frame and the C-core is conducted in accordance with the test procedure in section 3.2.1 and section 3.2.2. The measured losses in the SFT are presented in Table III. For the case of no plate, 1mm steel plate, and 2mm steel plate in the airgap, the combined losses will be used as a reference for the combined flux test.

TABLE III. Losses obtained in the SFT for the Epstein frame and C-core

Test	Epstein frame losses[W]	C-core losses[W]	Combined losses[W]
No plate	20.42	6.20	26.62
1mm plate	20.42	5.99	26.41
2mm plate	20.46	6.08	26.54

The measured core losses in Table III suggest that losses from the Epstein frame power loss measurement are not significantly affected by the introduction of steel plates in the airgap between the main core and the C-core. Although minor variations in C-core measured core losses are observed, a distinct trend for increasing steel plate thickness is not present in the SFT results in Table III. The variations in C-core measured power losses are reflected in the combined losses.

4.2.2 Artificial leakage flux test results

With the combined losses from the Epstein frame SFT and C-core SFT in Table III as reference losses, the incremental losses from the ALF test are presented in Figure 4.15 for increasing phase shift between applied voltages.

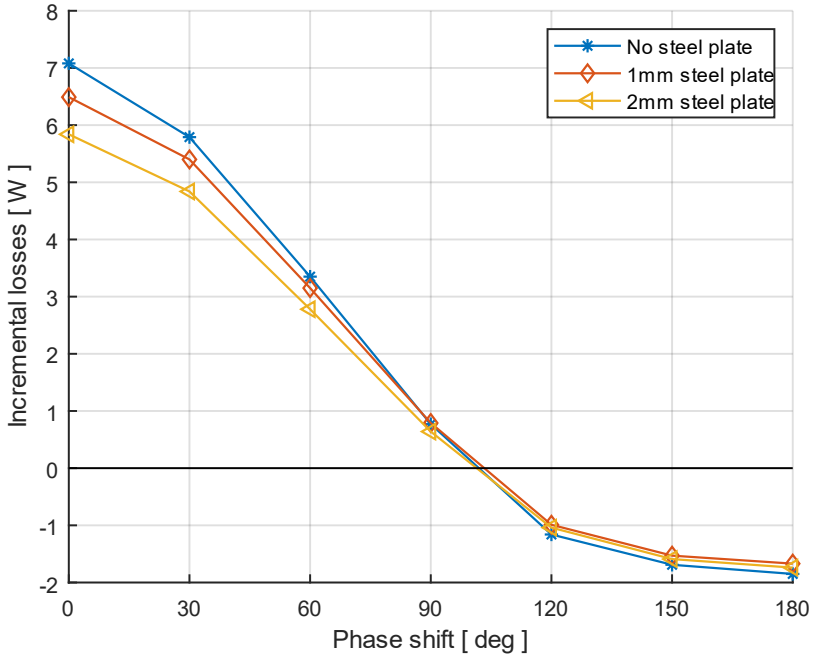

Figure 4.15. Results from the ALF test with no steel plate, 1mm steel plate and 2mm steel plate. Incremental loss is the deviation from the associated reference losses. Phase shift is the angle between excitation voltages.

There are observable differences between the ALF test without steel plate, ALF test with 1mm steel plate, and ALF test with 2mm steel plate in Figure 4.15. Incremental losses are increasing for decreasing steel plate thickness for phase shift angles between $\theta = 0°$ and $\theta = 90°$. However, the trend is not continuous for phase shift angles above 90°.

The incremental losses are highest for 0° phase shift angle, where the measured ALF test losses with no steel plate are 27% higher than the reference loss from Table III. At $\theta = 90°$, the ALF test incremental losses are close to the reference SFT losses. At $\theta = 180°$, the incremental losses are 7% lower than the associated SFT reference.

The incremental losses in the ALF test are the sum of losses measured in the Epstein frame and C-core watt-meter configuration. Figure 4.16 illustrates where the losses are obtained for increasing phase shift as a percentage of the combined losses.

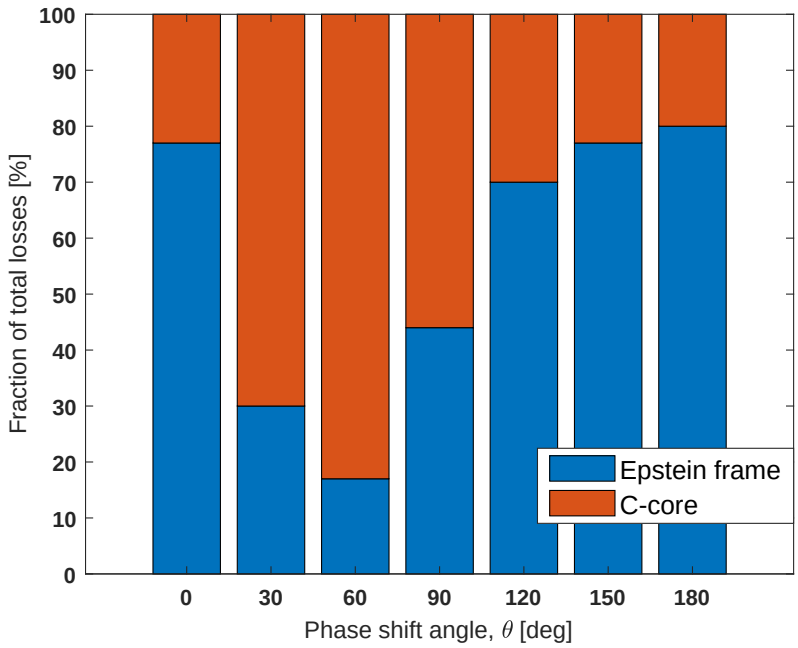

Figure 4.16. Results for the ALF test with no steel plate presenting the combined loss distribution as percentage of the total losses.

In Figure 4.16 only ALF test with no steel plate is presented. The difference in power loss distribution between the ALF test with a 1mm steel plate and a 2mm steel plate is negligible compared to the ALF test with no steel. Consequently, results for the ALF test with steel plates are not included in Figure 4.16. With a voltage phase shift of $\theta = 0°$, 77% of the total losses are obtained by the Epstein frame loss measurements, illustrated in Figure 4.16. The majority of losses are obtained in the C-core measurement for voltage phase angles of $\theta = 30°$ to $\theta = 90°$. At $\theta = 180°$, approximately 80% of losses are obtained in the Epstein frame measurement circuit. Figure 4.17 gives further insight into measurement results for the ALF test.

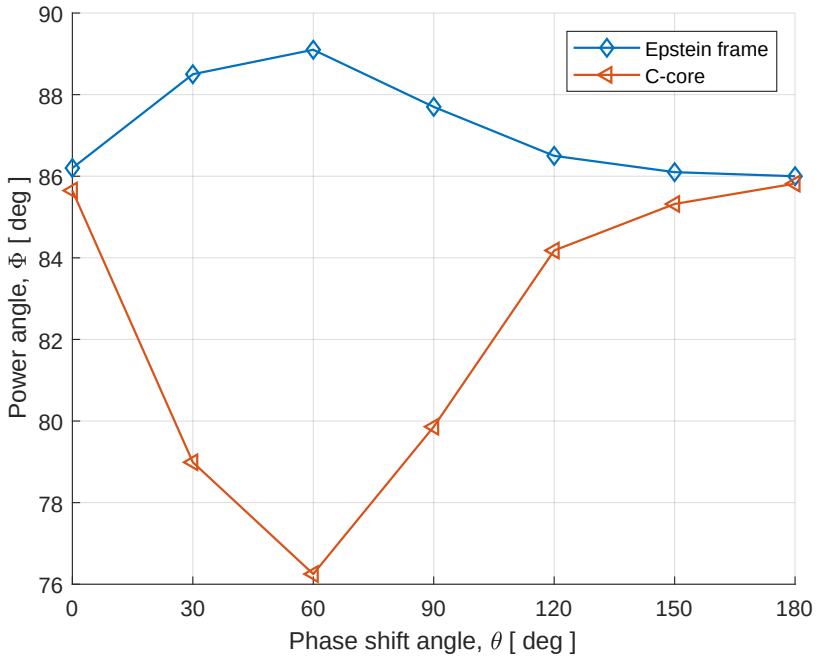

Figure 4.17. Results for the ALF test with no steel plate. Epstein frame power angle Φ_{Ep} and C-core power angle Φ_{Cc}.

The Epstein frame power angle Φ_{Ep} and the C-core power angle Φ_{Cc} are plotted in Figure 4.17 for increasing voltage phase shift. The Epstein frame power angle is increasing for phase shift angles up to $\theta = 60°$. This trend is reflected in the loss distribution chart in Figure 4.16, where losses obtained in the Epstein frame circuit relative to the total losses are reduced in the same interval. Similarly for the C-core measurements in the voltage phase angle interval $\theta = 0°$ to $\theta = 60°$, the power factor angle Φ_{Cc} is decreasing. In the same interval, the losses obtained by the C-core measurement circuit increase.

In the phase angle interval $\theta = 60°$ to $\theta = 180°$, the Epstein frame power angle Φ_{Ep} is decreasing whereas the C-core power angle Φ_{Cc} is increasing. The result correlates well with the loss distribution in Figure 4.16 where the relative losses increase in the Epstein frame circuit and decrease in the C-core circuit.

4.2.3 FEM model results

The FEM model is simulated with excitation similar to the real test setup, and the results are thus separated into single flux test results and artificial leakage flux test results. First, the SFT are test results are presented. The simulation results of the ALF test then described.

The FEM-SFT resulting magnetic flux density for the Epstein frame is presented in Figure 4.18 at selected time steps corresponding to peak excitation current in the Epstein frame winding for Figure 4.18(a) and for the C-core in Figure 4.18(b).

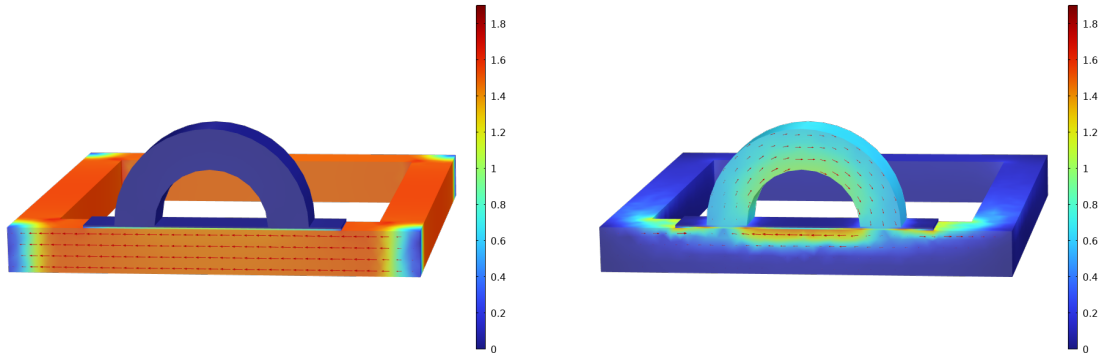

(a) **(b)**

Figure 4.18. Magnetic flux density plot with a range of 0T to 1.8T of the simulated SFT of: (a) the Epstein frame; (b) the C-core

The magnetic flux density in Figure 4.18(a) is close to uniformly distributed in most iron core cross-sections with the exception of corners, where the flux density is low. The average magnetic flux density in an arbitrary iron core cross-section inside the excitation windings is $B_{avg} = 1.54$T, correlating well with the desired magnetic flux density of 1.5T. Across an iron core cross-section located underneath the C-core, the average flux density is $B_{avg} = 1.44$T. Only a negligibly small amount of magnetic flux has a path in the C-core iron, with an average flux density in a cross-section of the C-core of $B_{avg} = 0.02$T at peak excitation current.

The magnetic flux density in the FEM-SFT of the C-core is shown in Figure 4.18. The magnetic flux density distribution is non-uniform in an arbitrary cross-section of the main iron core underneath the C-core. The top sheets in the Epstein frame form a high flux density region. The flux density is negligible in the bottom sheets of the main core in the FEM-SFT in Figure 4.18(b). For the C-core iron core, the magnetic flux density correlates well with the measured magnetic field in the real SFT of the C-core at $B_m = 0.8$T.

The combined flux test is simulated on the FEM 3D model at selected phase shift angles of excitation voltage. The FEM-test procedure is described in detail in section 3.2.5. Excitation voltage phase shifts of $\theta = 0°$, $\theta = 90°$ and $\theta = 180°$ is implemented in the model using the currents defined in Figure 3.22, resulting in the magnetic flux distribution in Figure 4.19.

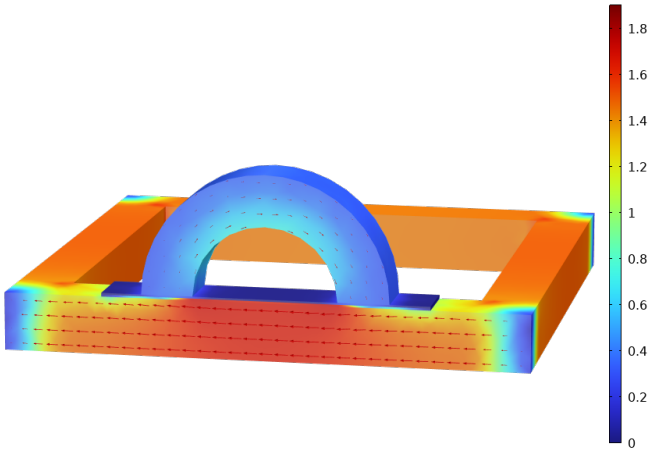

(a)

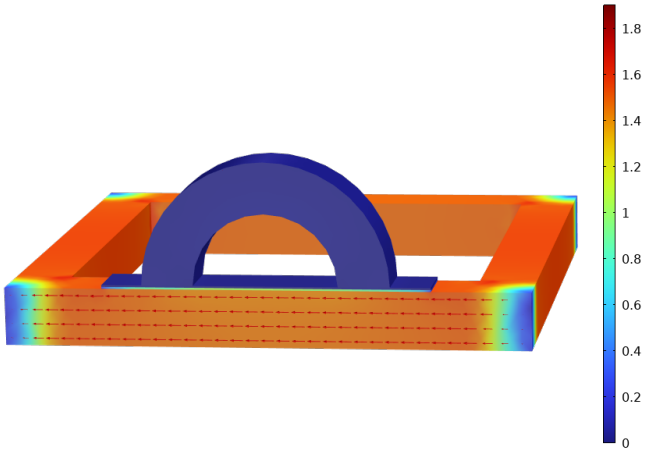

(b)

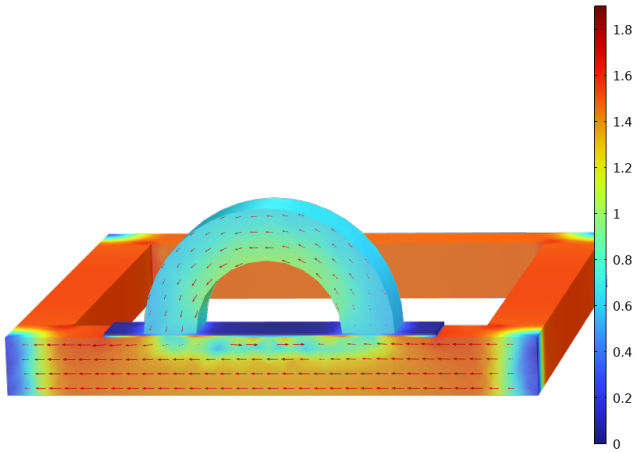

(c)

Figure 4.19. Magnetic flux density plot with a range of 0T to 1.8T for the FEM-ALF test evaluated at voltage phase shift of: (a) $\theta = 0°$; (b) $\theta = 90°$; (c) $\theta = 180°$.

Chapter 5

Discussion

Synchronous Generator Modelling

To validate that the 3D model is correctly implemented, a no-load test is performed on the 2D VSM and the simplified 3D model with field current corresponding to the selected operation points. The magnetic flux density norm comparison in Figure 4.1 indicates that the 2D and 3D simplified model produces similar magnetic flux densities. Similar results are observed for inspection of the magnetic flux density under loaded operation in Figure 4.5. In the no-load test, the magnitude of the induced voltage at all the selected operation points is observed to correlate well by comparing voltage waveforms in Figure 4.2 and Figure 4.3. There is observable harmonic distortion on the 2D induced no-load voltage waveform in Figure 4.3(a), visible also in the corresponding 3D model waveform in Figure 4.2(a). This distortion is not considered important for further analysis.

In addition to the induced voltage comparison, the magnetic flux radial component is investigated for the 2D model and simplified 3D model. From Figure 4.4 it is evident that only minor differences is present in the radial flux density. Similarly, only minor differences are observable under loaded operation, as illustrated in Figure 4.6. The small discrepancies are assumed to be related to the differences in mesh for the 2D and 3D model. The simplified 3D model utilized a much coarser mesh than the 2D model. The results are considered satisfactory. The no-load and loaded tests of the 3D simplified VSM model thus confirm that the implementation of the 3D VSM can be considered trustworthy.

Ideally, more tests would be preferable to validate the 3D model further. A torque comparison at all operating points would be valuable in this regard. However, the implementation of torque calculation in the 3D VSM and the 3D Simplified VSM is not done in this thesis. Accurate calculation of torque in 3D requires a considerably finer mesh than the mesh used in this thesis. Consequently, this analysis is not implemented considering the increased computational strain and the uncertainties involved.

When evaluating the end region flux density, end region axial flux density and associated end region losses are observed between operation points. The magnetic flux density is high at all operating points. This is because the end region leakage flux superimposes the main flux in the end region stator iron with a significant axial component. The cycle averaged eddy current losses in the pressing structure at leading power factor are more than three times the losses at unity power factor. The explanation is assumed to be related to the magnetic flux axial component. From the evaluation of eddy current density in the pressing structure in Figure 4.12, it is observed that the current density in both the pressing structure and stator iron is much higher in the case of leading power factor. The

axial flux density is higher at the leading power factor in Figure 4.10. However, the effect is not as significant for the axial component evaluated in the stator iron. It is worth noting that the current density is high in all operation points.

The effect of end region leakage flux is further described with a comparison of the magnetic flux density norm of the complete 3D VSM model in Figure 4.8 and for the simplified 3D VSM model. As the two models are identical regarding the selected operating point and time step, they are comparable. With the end windings removed, the magnetic flux density is similar to the 2D model representing an arbitrary cross-section.

Artificial Leakage Flux Test

The effect of magnetic leakage flux with a significant normal component is investigated for a wide range of flux phase shifts in the combined flux test. A single flux test is successfully performed on the Epstein frame and C-core and visualized using the FEM model. Negligible dc-offset and a 90° phase shift between obtained excitation current and induced voltage for both the Epstein frame SFT and the C-core SFT indicate that the test setup is suitable for conducting this test. The induced voltage in the Epstein frame SFT and the C-core SFT is purely sinusoidal, thus confirming that the assumption of sinusoidal flux density is valid.

The phase shift between the main core and C-core magnetic flux is observed to influence the incremental losses in the CFT. Figure 4.15 shows that losses are highest in the CFT when the main flux and C-core flux are in phase. The additional losses can be explained by saturation of the main core underneath the C-core, supported by the FEM model simulation of the CFT. The saturated region forms because of the interaction between the high flux density region from the C-core SFT and the main flux. When the two are completely in phase, an extended high flux density region is formed, visualized in Figure 4.19(a). By adjusting the phase shift to 90°, the losses in the CFT are close to the sum of losses of single flux tests. An interaction between the two fields is still present. However, the effect is insignificant at maximal excitation for the C-core and main core, following the excitation currents in Figure 3.22(b). The incremental losses are non-zero, indicating that there are regions of saturated core affecting the flux density in the real test. When the phase angle between C-core flux and the main flux is 180°, the losses are lower than the reference SFT losses. The simulation of this situation in Figure 4.19(c) illustrates how the C-core field opposes the main flux in the top sheets of the main core. The opposing field is leading to a significant reduction in magnetic flux density under the C-core.

The CFT is conducted with a stainless steel plate of varying thickness in the airgap. The losses are observed to decrease for increasing steel plate thickness in Figure 4.15. The reduced measured losses are related to the increased air gap length between tests. The total airgap length is increased from 1mm in the CFT with no steel plate to a total length of 3mm in the CFT with a 2mm steel plate. A constant airgap should thus be maintained to improve this test.

The FEM model of the test setup satisfactorily visualizes the real tests. However, some simplifications have been made. Inspection of the obtained waveforms from the Epstein frame circuit shows that a significant third harmonic component is present in the real excitation current, as shown in Figure 4.13. However, the excitation currents used in the simulated cases in Figure 3.22 are purely sinusoidal and are consequently not a valid representation of the real current. Furthermore, the secondary winding of both the C-core and the main core is not included in the simulation model, thus excluding possible

comparison of induced voltages. Improved implementation of the FEM model can be used to compare FEM losses to the experimentally obtained losses. Such comparison can verify that the FEM model is a valid representation of the real test setup. Furthermore, if successful, this comparison will support the assumption that the 3D VSM model is a valid representation of the real machine.

Chapter 6

Conclusions

In this thesis, a 3D FEM model of a real synchronous generator is created using software from COMSOL Multiphysics. Suitable adjustments to a real 100kVA generator's original stator design are proposed to minimize the required computational power for simulations. Comparisons between the 3D virtual synchronous machine (VSM) model and 2D VSM for loaded and no-load operations indicate that the 3D model is correctly implemented. Evaluation of end region losses is successfully conducted using the proposed 3D VSM model. The losses in the end region clamping plate and press fingers are significantly higher for under-excited operation than at unity power factor or over-excitation. The cycle averaged losses are more than three times higher at leading power factor than at unity power factor in the end region pressing structure.

Emulated leakage field tests are successfully conducted using an experimental approach with an Epstein frame and a C-core. From the test results, it can be concluded that the core losses are affected by introducing an external magnetic field emulating the end region leakage flux. By investigation of incremental losses, it is observed that the losses are sensitive to variations in the phase angle between the main field in the rolling direction and the external field in the normal direction.

Chapter 7

Suggested further work

There are several areas of possible improvement of the 3D VSM model and the artificial leakage flux test. Only three operations points are investigated in calculating end region losses, corresponding to leading, unity, and lagging power factor at 80kVA. Simulations of different operating points could be used to validate that the conclusions drawn here can be generalized.

The time-dependent studies on the 3D VSM model are time-consuming, with an average simulation time of 7.5 days for the 3D VSM when run to complete one single electrical period. Only minor time variances in losses are observed after an initial transient period, but a longer simulation time would help validate this. The mesh used in the 3D VSM could easily be improved by reducing the maximum element size in the stator iron, press fingers, and clamping plate, as well as a general reduction in element size, to further increase the accuracy of results. Furthermore, a finer mesh could make it possible to implement torque calculations in the 3D model. For this, the simplified 3D VSM model should be used to neglect the effect of end winding flux. If successful, such analysis would increase the trustworthiness of the generator model.

Ideally, the losses obtained in this thesis would be compared to experimentally obtained losses in the RSM end region. However, such analysis is difficult to conduct in practice. Alternatively, a possible validation method could be to compare the obtained ALF test core losses to FEM model losses. The proposed 3D FEM model of the Epstein frame and C-core must be improved to accomplish this. An improved model should include different excitation methods, finer mesh, and a core loss calculation. Although this is straightforward, other aspects have been prioritized in this thesis. The artificial leakage flux test could be improved by maintaining a constant airgap length between the main flux core and the leakage flux core for varying steel plate thickness.

Bibliography

[1] P.J. Tavner and A.F. Anderson. "Core faults in large generators". In: *Electric Power Applications, IEE Proceedings* - 152 (Dec. 2005), pp. 1427–1439. DOI: 10.1049/ip-epa:20050102.

[2] B.C. Mecrow, A.G. Jack, and C.S. Cross. "Turbogenerator electromagnetic design-the design of eddy current shields for screening of end-regions". In: *1989 Fourth International Conference on Electrical Machines and Drives Conf. Publ. No. ??)* 1989, pp. 111–115.

[3] Sufei Li et al. "Analyzing the impact of press plate structure on the flux and loss distributions in the end region of large generators by transient 3-dimensional finite-element method with an improved core loss model". In: *2017 IEEE International Electric Machines and Drives Conference (IEMDC)* (2017), pp. 1–8.

[4] Sufei Li et al. "Analyzing the impact of press plate structure on the flux and loss distributions in the end region of large generators by transient 3-dimensional finite-element method with an improved core loss model". In: *2017 IEEE International Electric Machines and Drives Conference (IEMDC)*. 2017, pp. 1–8. DOI: 10.1109/IEMDC.2017.8002363.

[5] Birger Marcusson and Urban Lundin. "Axial Magnetic Fields at the Ends of a Synchronous Generator at Different Points of Operation". In: *IEEE Transactions on Magnetics* 51.2 (2015), pp. 1–8. DOI: 10.1109/TMAG.2014.2347269.

[6] Børge Johannes Fagermyr. *Influence of compressive stress on non-oriented electrical steel in the stacking direction*. Project report in TTM4520. Department of Electric Power Engineering, NTNU – Norwegian University of Science and Technology, Dec. 2021.

[7] *Power system dynamics Stability and Control*. John Wiley & Sons, Inc., 111 River Street, Hoboken, NJ 07030, USA: Wiley, 2020.

[8] NICOLA BIANCHI. *Electrical Machine Analysis Using Finite Elements (Power Electronics and Applications Series*. POWER ELECTRONICS AND APPLICATIONS SERIES. CRC Press Taylor & Francis Group, 2005. ISBN: 0849333997.

[9] Andreas Krings and Juliette Soulard. "Overview and Comparison of Iron Loss Models for Electrical Machines". In: *Journal of Electrical Engineering* 10 (May 2010), pp. 162–169.

[10] Charles Proteus Steinmetz. "On the law of hysteresis". In: *Proceedings of the IEEE* 72 (1984), pp. 197–221.

[11] Jiancheng Fang and Shilei Xu. "Effects of Eddy Current in Electrical Connection Surface of Laminated Cores on High-Speed PM Motor Supported by Active Magnetic Bearings". In: *IEEE Transactions on Magnetics* 51.11 (2015), pp. 1–4. DOI: 10.1109/TMAG.2015.2449905.

[12] Wei Wang, Arne Nysveen, and N. Magnusson. "Apparatus for loss measurements under multidirectional and dc-bias flux in electrical steel laminations". In: *Review of Scientific Instruments* 91 (Aug. 2020), p. 084705. DOI: 10.1063/5.0011076.

Appendix A

Appendix

A.1 B-H curve for S275N magnetic steel

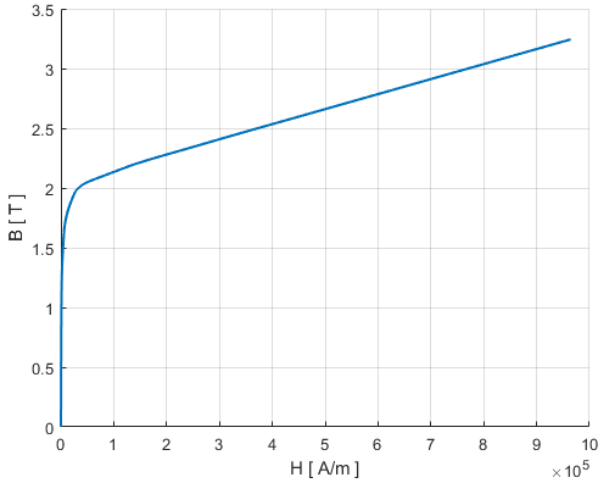

Figure A.1. BH-curve used for modelling the end region support structure.

A.2 Winding layout RSM

TABLE I. Winding layout for the RSM corresponding to half of the total machine

Slot number	**1**	**2**	**3**	**4**	**5**	**6**	**7**	**8**	**9**	**10**	**11**	**12**	**13**	**14**	**15**	**16**	**17**	**18**	**19**
Top layer	R	R	R	-T	-T	-T	S	S	S	-R	-R	T	T	T	-S	-S	-S	R	R
Bottom layer	R	R	-T	-T	-T	S	S	-R	-R	-R	T	T	T	-S	-S	-S	R	R	-T

Slot number	**20**	**21**	**22**	**23**	**24**	**25**	**26**	**27**	**28**	**29**	**30**	**31**	**32**	**33**	**34**	**35**	**36**	**37**	**38**
Top layer	-T	-T	-T	S	S	S	-R	-R	-R	T	T	-S	-S	-S	R	R	R	-T	-T
Bottom layer	-T	-T	S	S	S	-R	-R	T	T	T	-S	-S	-S	R	R	R	-T	-T	S

Slot number	**39**	**40**	**41**	**42**	**43**	**44**	**45**	**46**	**47**	**48**	**49**	**50**	**51**	**52**	**53**	**54**	**55**	**56**	**57**
Top layer	S	S	S	-R	-R	-R	T	T	T	-S	-S	R	R	R	-T	-T	-T	S	S
Bottom layer	S	S	-R	-R	-R	T	T	-S	-S	-S	R	R	R	-T	-T	-T	S	S	-R

A.3 Permeability curve M400-50A

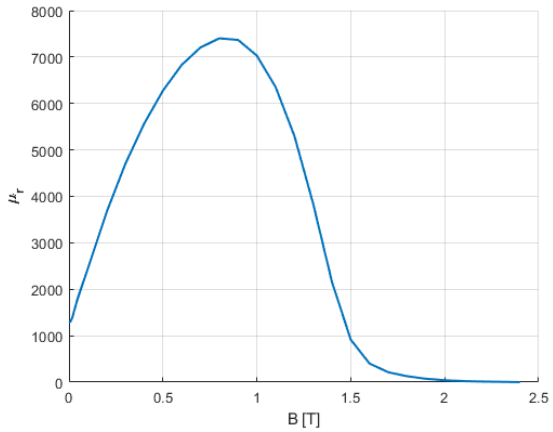

Figure A.2. Relative permeability curve for non-oriented electrical steel grade M400-50A.

A.4 Phasor diagram calculated values

	OP1		OP2		OP3	
Quantity	Magn [pu]	*Angle*[°]	Magn [pu]	*Angle*[°]	Magn [pu]	*Angle*[°]
EQ	0.7057	59.22	1.153	29.86	1.8972	18.626
Eq	0.8396	59.22	1.2638	29.86	2.556	18.626
I	1.1744	46.52	0.7656	0.00	1.3358	-53
Iq	1.1457	59.22	0.6639	29.86	0.4258	18.626
Id	0.2582	-30.78	0.38123	-60.14	1.2661	-71.374

A.5 Data sheet BH-curve for M300-35A

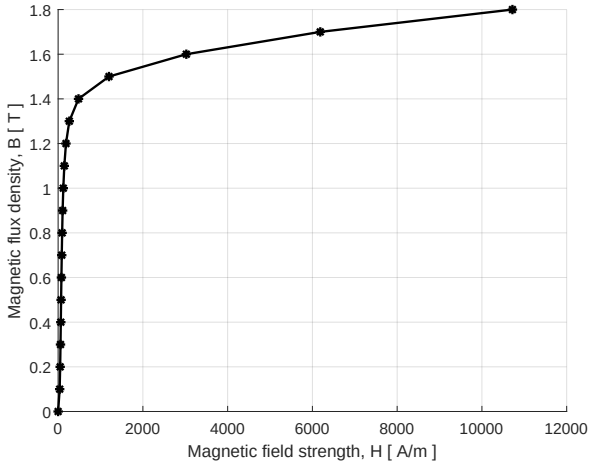

Figure A.3. BH-curve for M300-35A.

A.6 Obtained C-core BH-curve from SFT

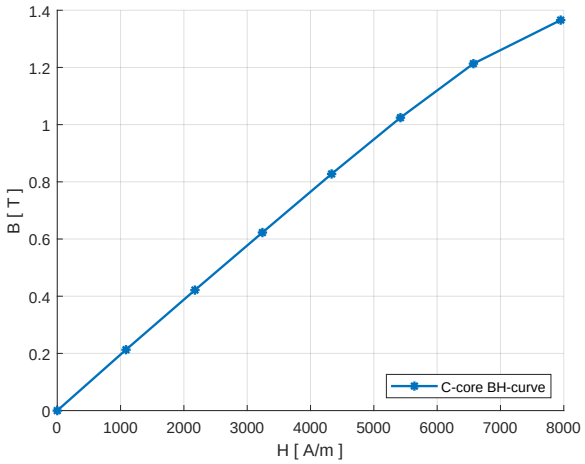

Figure A.4. C-core SFT BH-curve

A.7 M400-50A Sura datasheet

Typical data for SURA® M400-50A

T	W/kg at 50 Hz	VA/kg at 50 Hz	A/m at 50 Hz	W/kg at 100 Hz	W/kg at 200 Hz	W/kg at 400 Hz	W/kg at 1000 Hz	W/kg at 2500 Hz
0,1	0,02	0,07	32,6	0.07	0.16	0,48	2.12	8.64
0,2	0,09	0,18	43,5	0.26	0.64	1,80	7.49	30.1
0,3	0,19	0,33	50,8	0.54	1.35	3,77	15.3	62.7
0,4	0,31	0,50	57,2	0.88	2.25	6,29	25.7	109
0,5	0,46	0,69	63,4	1.27	3.33	9,37	39.0	172
0,6	0,62	0,91	69,9	1.73	4.58	13,1	56.1	256
0,7	0,81	1,16	77,3	2.24	6.03	17,5	77.1	367
0,8	1,01	1,46	86,0	2.80	7.68	22,7	103.1	509
0,9	1,24	1,81	97,2	3.44	9.58	28,8	135.0	685
1,0	1,49	2,23	113,2	4.15	11.7	35,9	173.3	899
1,1	1,76	2,79	137,8	4.95	14.2	44,2	218.8	1155
1,2	2,09	3,60	180,2	5.85	17.0	53,8	272.4	1453
1,3	2,46	5,07	269,5	6.88	20.2	64,9	334.6	1793
1,4	2,96	8,80	516,8	8.18	23.8	77,4	405.6	2130
1,5	3,57	21,6	1307	9.82	28.3	91,7	488.4	
1,6	4,38	57,2	3180					
1,7	5,02	128	6361					
1,8	5,47	243	10890					

Loss at 1.5 T , 50 Hz, W/kg	3,57
Loss at 1.0 T , 50 Hz, W/kg	1,49
Anisotropy of loss, %	8
Magnetic polarization at 50 Hz	
H = 2500 A/m, T	1,59
H = 5000 A/m, T	1,68
H = 10000 A/m, T	1,79
Coercivity (DC), A/m	50
Relative permeability at 1.5 T	1050
Resistivity, μΩcm	42
Yield strength, N/mm²	325
Tensile strength, N/mm²	465
Young's modulus, RD, N/mm²	200 000
Young's modulus, TD, N/mm²	210 000
Hardness HV5 (VPN)	165

RD represents the rolling direction
TD represents the transverse direction
Values for yield strength (0.2 % proof strength)
and tensile strength are given for the rolling direction
Values for the transverse direction are approximately 5% higher

cogent
Surahammars Bruks AB

Oct 2009

A.8 M300-35A Sura datasheet

Typical data for SURA® M300-35A

T	W/kg at 50 Hz	VA/kg at 50 Hz	A/m at 50 Hz	W/kg at 100 Hz	W/kg at 200 Hz	W/kg at 400 Hz	W/kg at 1000 Hz	W/kg at 2500 Hz
0,1	0,03	0,07	30,9	0,04	0,09	0,23	1,07	4,45
0,2	0,08	0,17	40,2	0,17	0,40	1,00	4,08	16,1
0,3	0,15	0,30	46,4	0,35	0,85	2,15	8,48	33,6
0,4	0,24	0,45	52,1	0,58	1,41	3,61	14,0	56,9
0,5	0,35	0,62	57,9	0,84	2,06	5,36	20,9	86,6
0,6	0,48	0,82	64,4	1,14	2,81	7,42	29,2	124
0,7	0,61	1,05	72,0	1,46	3,66	9,75	39,0	170
0,8	0,76	1,31	81,1	1,83	4,61	12,4	50,6	227
0,9	0,92	1,63	92,6	2,23	5,65	15,4	64,1	297
1,0	1,10	2,03	108	2,66	6,80	18,8	79,8	382
1,1	1,30	2,55	130	3,16	8,09	22,5	98,0	
1,2	1,54	3,32	168	3,72	9,54	26,8		
1,3	1,82	4,71	250	4,39	11,2	31,6		
1,4	2,20	8,61	510	5,23	13,4	37,7		
1,5	2,62	23,7	1440	6,22	15,7	44,3		
1,6	2,98	64,1	3490					
1,7	3,25	138	6700					
1,8	3,41	255	11300					

Loss at 1.5 T , 50 Hz, W/kg	2,62
Loss at 1.0 T , 50 Hz, W/kg	1,10
Anisotropy of loss, %	10
Magnetic polarization at 50 Hz	
H = 2500 A/m, T	1,55
H = 5000 A/m, T	1,65
H = 10000 A/m, T	1,78
Coercivity (DC), A/m	45
Relative permeability at 1.5 T	830
Resistivity, μΩcm	50
Yield strength, N/mm²	370
Tensile strength, N/mm²	490
Young's modulus, RD, N/mm²	185 000
Young's modulus, TD, N/mm²	200 000
Hardness HV5 (VPN)	185

RD represents the rolling direction
TD represents the transverse direction
Values for yield strength (0.2 % proof strength)
and tensile strength are given for the rolling direction
Values for the transverse direction are approximately 5% higher

cogent
Surahammars Bruks AB

June 2008